



**HAL**  
open science

## Recent trends in the wind-driven California current upwelling system

Yves Quilfen, J. Shutler, Jean-Francois Piolle, Emmanuelle Autret

► **To cite this version:**

Yves Quilfen, J. Shutler, Jean-Francois Piolle, Emmanuelle Autret. Recent trends in the wind-driven California current upwelling system. *Remote Sensing of Environment*, 2021, 261, 112486 (17p.). 10.1016/j.rse.2021.112486 . hal-04203463

**HAL Id: hal-04203463**

**<https://hal.science/hal-04203463>**

Submitted on 22 Jul 2024

**HAL** is a multi-disciplinary open access archive for the deposit and dissemination of scientific research documents, whether they are published or not. The documents may come from teaching and research institutions in France or abroad, or from public or private research centers.

L'archive ouverte pluridisciplinaire **HAL**, est destinée au dépôt et à la diffusion de documents scientifiques de niveau recherche, publiés ou non, émanant des établissements d'enseignement et de recherche français ou étrangers, des laboratoires publics ou privés.



Distributed under a Creative Commons Attribution - NonCommercial 4.0 International License

2  
4  
6  
8  
10  
12  
14  
16  
18  
20  
22  
24  
26  
28  
30  
32  
34  
36  
38  
40  
42  
44

# Recent trends in the wind-driven California Current Upwelling System

Y. Quilfen<sup>1</sup>, J. Shutler<sup>2</sup>, J.-F. Piolle<sup>1</sup>, E. Autret<sup>1</sup>

<sup>1</sup>IFREMER, Univ. Brest, CNRS, IRD, Laboratoire d'Océanographie Physique et Spatiale (LOPS), IUEM, Brest, France  
<sup>2</sup>College of Life and Environmental Sciences, University of Exeter, Penryn, UK

Corresponding author: Yves Quilfen (Yves.Quilfen@ifremer.fr)

## Highlights:

- The seasonal upwelling transport has increased by as much as 25% in 1996-2018
- Spatially structured trends in pH and Chl-a are observed for the same period
- Results from satellite analysis and model reanalysis products diverge locally

46 **Abstract**

48 Long-term changes in the marine ecosystems of the Eastern Boundary Upwelling Systems  
50 (EBUS) are predicted due to anthropogenic climate change. In particular, global ocean  
acidification is having a profound effect on the coastal waters of the EBUS, affecting the entire  
52 trophic chain, net primary production (NPP) and related economic activities such as fisheries.  
Another predicted change related to human activity is that of upwelling dynamics with expected  
54 long-term changes in upwelling winds as proposed by Bakun (1990), Bakun et al. (2015) and  
Rykaczewski et al. (2015). Although these predicted long-term changes may emerge only later in  
56 the 21<sup>st</sup> century, this has fueled many studies using historical data. Long-term increase in  
upwelling winds has thus been a much debated topic, showing that there is considerable  
58 uncertainty depending on the EBUS considered, the effect of natural climate fluctuations, the  
choice of wind dataset, the time period considered, and the methodologies and significance tests  
60 applied. Therefore, there is an immediate interest in being able to monitor upwelling using  
verified and self-consistent wind data sets. This work focused on a sensitivity study of the  
62 estimated trends in upwelling winds in the California Current Upwelling System (CCUS), for the  
most recent period 1996-2018, using the two state-of-the-art satellite wind analyses and two  
64 atmospheric model re-analyses. Embedded into the strong modulation by natural climate  
fluctuations on interannual and decadal time scales, we do see an increase in upwelling-favorable  
winds in the core of the CCUS, with a local increase of more than 25% in seasonal upwelling  
66 transport for the period considered. In this central upwelling zone, a good agreement on stronger  
equatorward winds for the winter and spring seasons is found between the different datasets,  
68 although with different significance levels. Conversely, conflicting results are found in the  
southernmost part of the CCUS between the satellite analyses and the model reanalyses.

70 Systematic, time-dependent differences are found between the wind products, highlighting the  
need to further investigate the poorly documented temporal stability of these widely used wind  
72 long-term climatology products. The observed spatial structuring of the estimated wind trends is  
consistent with the trend analysis of water chlorophyll-a, partial pressure of CO<sub>2</sub>, and basity (pH)  
74 analysis products. This result is consistent with changes being important for modulating the  
carbonate system within the CCUS.

76

### **1. Introduction**

78 EBUS are very active biogeochemical systems, which adapt to the timing and strength of  
upwelling winds whose natural variability extends over various spatial and temporal scales.  
80 Ecosystem productivity responds to this external forcing in complex ways, raising several  
unresolved questions and issues regarding the future of the coastal upwelling ecosystem and the  
82 global carbon cycle, as explained by Di Lorenzo (2015). Although there is past evidence that  
these upwelling ecosystems are resilient to natural changes in ocean-atmosphere dynamics such  
84 as those associated with El Niño events in the CCUS, there is great uncertainty about how these  
EBUS may respond to a long-term increase in the mean magnitude of upwelling winds and ocean  
86 stratification due to climate change (García-Reyes et al., 2015). Indeed, increased coastal  
upwelling in parts of the four eastern boundary upwelling systems has been predicted as a result  
88 of a deterministic and predictable increase in the contrast between atmospheric pressure over the  
ocean and land (Bakun, 1990), and/or as a result of a long-term poleward shift of ocean high  
90 pressure systems (Bakun et al., 2015; Rykaczewski et al., 2015). In addition, ocean acidification  
and deoxygenation are occurring within upwelling ecosystems (e.g. Feely et al., 2008; Gruber et  
92 al., 2012; Deutsch et al., 2020), likely driven by long-term global uptake of atmospheric CO<sub>2</sub> by

the ocean. However, clearly it is essential to understand how long-term changes in upwelling  
94 winds, that draw up water with distinctly different carbonate properties from depth, will also  
contribute to increased acidification and biogeochemical development of EBUS.

96 Numerous studies on trends in upwelling winds (e.g. Rykacewski and Checkley, 2008; Narayan  
et al., 2010; García-Reyes and Largier, 2010; Iles et al., 2012) followed the Bakun's (1990)  
98 article, fueled by the anticipated effects on coastal ecosystems and the global carbon cycle.  
Sydeman et al. (2014) conducted a meta-analysis of different past studies to discuss the  
100 consistency of the local long-term intensification of upwelling winds, and the contrasting results  
related to the choice of the period and duration studied, the effects of natural climate variability  
102 (interannual and lower frequency), the effects of seasonality, changes in instrumentation and the  
scarcity of spatially resolved observations, differences in the reporting of the statistical  
104 significance of trends, and differences in the results of model reanalyses and observations used.  
Furthermore, recent studies have identified that an increase in upwelling winds in a warming  
106 climate would be likely for only three of the EBUS (Wang et al., 2015), but not for the California  
upwelling, or that long-term changes in upwelling will emerge only late in the 21<sup>st</sup> century  
108 (Brady et al., 2017). Rykaczewski et al. (2015), using an ensemble of ocean-atmosphere coupled  
models, show the relationship between poleward migration of major ocean high pressure systems  
110 and changes in upwelling winds along the four EBUS, with spatial and temporal structuring of  
the predicted changes. Summer upwelling winds are predicted to intensify in the poleward area  
112 and weaken in the equatorward area, but with differing significant levels. Thus, they found  
equivocal results in the northern part of the CCUS and a significant decrease in upwelling winds  
114 in the southern part. While these modelling studies can cover very long time scales to provide  
results consistent with the scale of projected changes, there is also an immediate interest in

116 continuously monitoring actual changes with newly developed or improved wind climatology.  
Indeed, former atmospheric model reanalyses used in many upwelling trend studies may be  
118 affected by systematic biases (e.g. Belmonte and Stoffelen, 2019; Taboada et al., 2019). In the  
present study, we intend to elaborate on this topic, addressing the various issues related to the  
120 recent period and the CCUS, especially those dealing with data caveats, which have been  
overlooked in most studies. Our approach is therefore based on a sensitivity study using surface  
122 winds from recent model re-analyses and satellite analyses over the period 1996-2018 for which  
satellite winds provide a reliable spatially-resolved wind dataset (both in speed and direction).  
124 This temporal period also corresponds to a relatively neutral phase of the most important climate  
signals in the Pacific Ocean. In particular, we intend to highlight the essential role that satellite  
126 measurements can now play and in the future as a reliable source of baseline data, to help  
understand the evolution and variations within these upwelling systems, a concept that has  
128 proposed by previous studies but is yet to be demonstrated (Land et al., 2015, 2019; Shutler et al.,  
2019).

130 Section 2 provides a description of the data sets used, a comparative analysis of the different  
wind data sets, and most importantly a discussion of the data issues. Section 3 details the  
132 methodology used to characterize the intensity and phenology of upwelling along the California  
coast, as well as the methods applied to extract trends from time series. Section 4 aims to provide  
134 a quantitative assessment of trends for some of the key biogeochemical system parameters (i.e.  
chlorophyll-a, Chl-a, partial pressure of CO<sub>2</sub> (pCO<sub>2</sub>) and basity or pH) and an assessment of the  
136 annual and seasonal upwelling winds, with emphasis on their spatial structuring. In section 5, we  
highlight the changes in the phenology of upwelling winds associated with the main Pacific  
138 Ocean climate signals, in order to better analyze the interannual to near-decadal variability into

which a long-term trend of seasonal upwelling winds is shown to be embedded. A discussion  
140 follows in section 6 to analyze the main results and a summary is given.

## 2. Data

### 142 2.1 Wind data sets

To assess the validity, strengths and weaknesses of our analysis, we have conducted a sensitivity  
144 study of our results obtained with different data sources, each with specific characteristics and  
limitations. Indeed, spurious climate signals can be introduced by the interaction between any  
146 biases in the atmospheric numerical model and the evolving observing system, which is a major  
concern in climate reanalysis (Hersbach and al., 2018). It is also challenging for multi-satellite  
148 gridded products to achieve the accuracy required for climate studies (Bourassa et al., 2019). We  
therefore used four popular wind datasets: two satellite surface wind analyses, the Cross-  
150 Calibrated Multi-Platform (hereafter CCMP, Atlas et al., 2011; Mears et al., 2019) version 2.0  
and the Copernicus Marine Environmental Services (hereafter CMEMS, Bentamy and Croize-  
152 Fillon, 2012; Desbiolles et al., 2017), and two atmospheric re-analyses, ERAInterim (hereafter  
ERA-Interim, Dee et al., 2011) and its follow-on ERA5 (Hersbach et al., 2020). The choice to add ERA-Interim,  
154 although considered of lower quality than ERA5, is made because most recently published  
studies have used ERA-Interim and because it is also used as background or first guess to help find a  
156 consistent wind field in satellite data gaps in both the CCMP and CMEMS analyses. The  
European Center for Medium Range Weather Forecast (ECMWF) produced native reduced-  
158 Gaussian grids for ERA5 at 31 km resolution and for ERA-Interim at 80 km resolution, which  
have been remapped by ECMWF at 0.25° and 0.5° grid resolution, respectively, for distribution  
160 by the Copernicus Climate Change Service. The four datasets are averaged at daily resolution  
using the available fields every 6 hours. Both CCMP and CMEMS have a resolution of 0.25° in

162 latitude and longitude, and use different sets of radiometer and scatterometer sensors with cross-  
calibration and editing of data performed independently by each data provider. The CCMP and  
164 CMEMS products are derived from very different mapping analysis, a geostatistical analysis is  
used for the CMEMS products and a variational analysis for the CCMP products, but both use the  
166 ERAI winds as background. It is worth noting that, unlike the CCMP analysis, the CMEMS  
products do not assimilate buoys wind data and do not calculate winds over land areas. This  
168 allows independent assessment in studies using buoy as reference (e.g. Kent et al., 2013;  
Carvalho et al., 2014; Desbiolles et al., 2017; Wang et al., 2019; Taboada et al., 2019), avoids  
170 artifacts in the calculation of wind stress curl at locations close to buoys (Mears et al., 2019), and  
gives a weaker dependency on ERAI numerical winds. Indeed, near the coast, a 25-50 km blind  
172 zone exists for satellite winds that makes the CCMP coastal winds more influenced by ERAI land  
winds since CCMP also calculates winds over land.

174 As any temporal trend analysis is very sensitive to the start and end points of the temporal record,  
the period analyzed in this study is limited to the period 1996-2018 in order to optimize the  
176 coverage of the region by scatterometers (ERS-1 and ERS-2 scatterometers in service at the  
beginning of 1996) and because the start and end of the period correspond to relatively calm  
178 periods for basin-scale climate variability. As only scatterometers provide near global coverage  
of wind direction, our choice of the period is therefore intended to limit the potential impact of  
180 the large ERAI wind biases (Belmonte and Stoffelen, 2019), within the CMEMS and CCMP  
products.

182 The winds used are equivalent neutral winds at ten-meter height, and the wind stress is derived  
for the four wind datasets using the neutral drag coefficient proposed in Hersbach (2011).

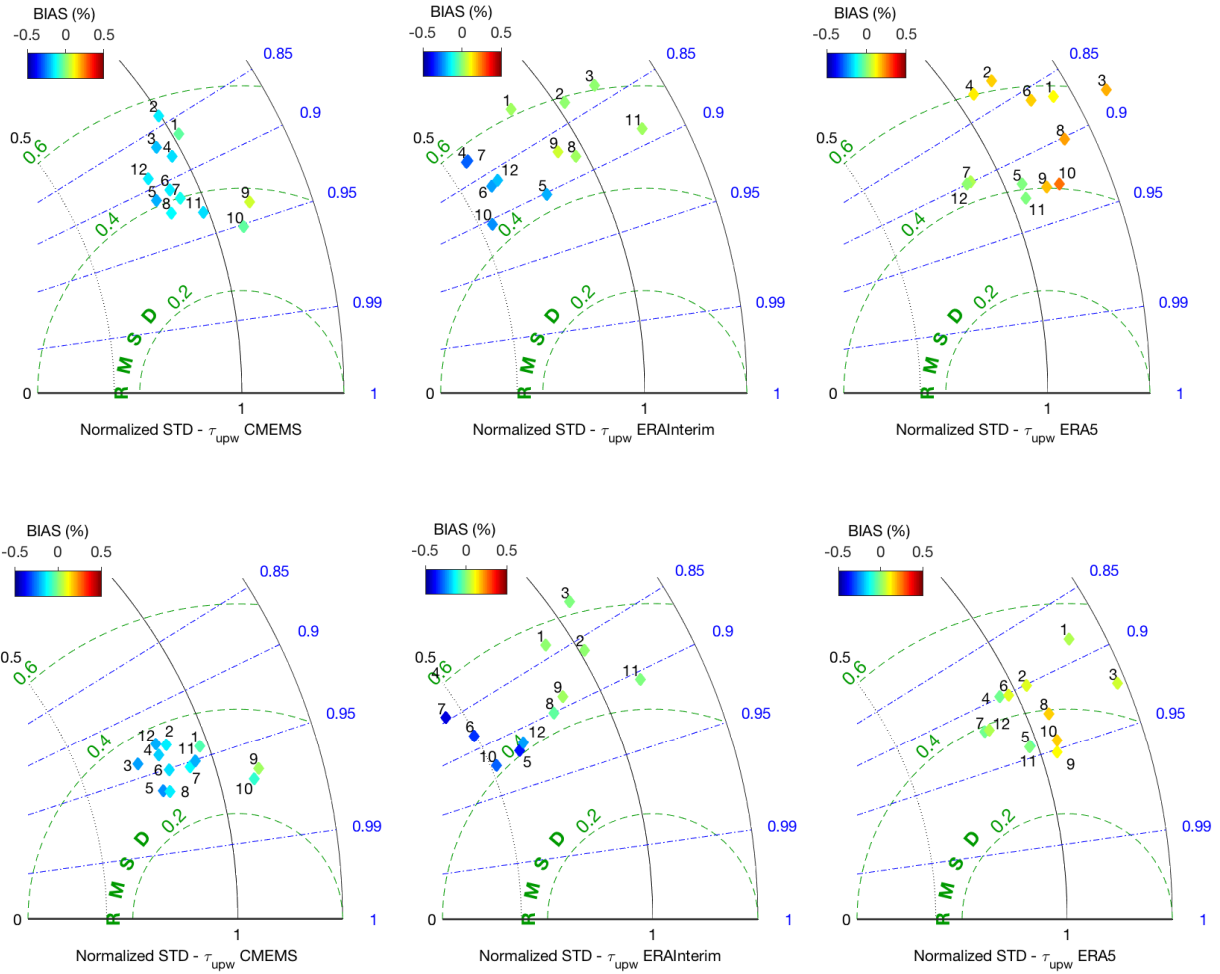
184

## 2.2 Comparison of wind data sets and data issues

186 Figure 1 presents a comparison using Taylor diagram analysis of the daily alongshore upwelling  
winds,  $\tau_{upw}$ , for the four data sources and twelve monitoring stations shown in Figure 2 and  
188 described in Appendix, Table A1. To facilitate the visualization of the Taylor diagram, the  
CCMP winds are the reference to which each of the other three is compared, as they have an  
190 overall medium level of variance among the four data sets. For each station, represented by the  
diamond symbols in Figure 1, the data are normalized using the corresponding CCMP standard  
192 deviation, so that a normalized standard deviation less (greater) than 1 indicates a lower (greater)  
level of variance in upwelling winds relative to the CCMP. The results can be summarized as  
194 follows: 1) there is a small dispersion (root mean square difference, RMSD) between CCMP and  
CMEMS satellite winds, and a larger dispersion between satellite and model reanalysis winds; 2)  
196 CMEMS winds have slightly lower mean winds and variance; 3) significantly lower mean winds  
and variance are observed for the ERAI at several stations; 4) significantly higher mean winds  
198 and variance are observed for the ERA5 at almost all stations; 5) comparison statistics improve  
for the second half of the period, except for the ERAI, which may be the result of greater  
200 assimilation of satellite data (in particular the Advanced SCATerometers, ASCAT) in the various  
processes of estimating wind climatology. Note as an important feature for the following  
202 analyses, the positive wind biases of the ERA5 are strongly reduced for the second half of the  
temporal period.

204

206



208

210 **Figure 1.** Taylor diagrams for comparison of CMEMS (left panels), ERAInterim (center panels),  
 212 ERA5 (right panels)  $\tau_{upw}$  with the CCMP data. The radial axis represents the normalized  
 214 standard deviation (STD), with the unit value referenced as the CCMP STD; the root mean  
 square differences (RMSD) with respect to the CCMP data are represented by green dashed  
 arcs and numbers ( $Nm^{-2}$ ); the correlation coefficients vary in the azimuthal direction as blue  
 dashed-dotted lines and numbers; and the diamonds are color-coded according to the mean bias  
 216 with respect to the CCMP ( $Nm^{-2}$ ). Top: 1996-2006; Bottom 2007-2018.

Complementary results are provided by an Empirical Orthogonal Function (EOF) analysis  
218 (Appendix A, Figures A1 and A2), in order to better describe the biases shown in Figure 1  
between CCMP and ERA5 and their dependence on time. This analysis is applied on the monthly  
220 meridional wind stress component over the ocean-only study area. The mean seasonal cycle has  
not been removed because there are strong latitude-dependent time shifts in the seasonality of  
222 winds. Consequently, the EOF decomposition divides the field variance into three most  
significant functions representing more than 92% of the total variance, each representing a part of  
224 the study area with different time scales and phases. Overall, Figure A1 shows that the spatial  
patterns fit well for the CCMP and ERA5. The first EOF, EOF-1, with more than 65% of the total  
226 variance, is the leading EOF north of 38°N and explains the strong seasonality of offshore  
meridional winds. At station 9, near 40°N, where EOF-1 accounts for about 95% of the wind  
228 variance, (Figure A2, top panel), shows that the mean difference between the ERA5 and CCMP  
meridional wind stress series, reconstructed from EOF-1, is almost constant with time. The third  
230 EOF, EOF-3, accounts for only about 4% of the total variance due to low seasonality, but is the  
leading EOF for the coastal ocean offshore Baja California and accounts for 49.5% and 56% of  
232 the total variance at station 4 near 30°N for the CCMP and ERA5, respectively. At station 4,  
there is little change over time in the difference between ERA5 and the CCMP when EOF-1 and  
234 EOF-2 are used to reconstruct the meridional wind stress series (Figure A2, center panel), but a  
large change is observed when EOF-3 is added (Figure A2, bottom panel), that accounts for 56%  
236 and 49.5% of the variance at this station for ERA5 and CCMP, respectively. The ERA5 winds  
show increased temporal variance but also a stronger pattern showing opposite phase between the  
238 coastal ocean offshore Baja California and the Gulf of California. These regional differences  
between ERA5 and CCMP explain the mean biases shown in Figure 1 and their evolution over

240 time, and this raises the immediate question of temporal homogeneity of the data for the different  
data sources.

242 Indeed, although each of the wind products used in our study was developed with the objective of  
ensuring temporal consistency, it is poorly documented and this consistency is therefore possibly  
244 unverified regionally. For satellite data, the development of climate data records for each  
instrument is indeed a recent concern. It is therefore challenging for multi-satellite gridded  
246 products to achieve the long-term consistency, precision and accuracy required for climate  
studies (Bourassa et al., 2019). The challenge is related to the evolution of the observing systems  
248 that makes difficult cross-calibration of the different instruments, but also to the fact that the two  
main multi-satellite products are dependent on another data source, i.e. the ERAI winds. To  
250 illustrate the problem, it is stated on the data producer web page that the CCMP winds should not  
be used for studying global trends, but are suitable for studying regional trends, due to the use of  
252 ERAI winds in the variational analysis scheme (<http://www.remss.com/measurements/ccmp/>). In  
addition, Desbiolles et al. (2017), although facing the same issue as the CCMP with the use of  
254 ERAI winds in the CMEMS products gridding process, conducted a global trend analysis whose  
results are presented as consistent with other data sources and showed better comparison statistics  
256 than the ERAI to buoys and QuikScat scatterometer. They note, however, that their products  
cannot be considered as being independent of ERAI. In addition, known effects may induce  
258 systematic differences between model reanalysis and satellite analysis products. Indeed,  
environmental factors such as surface currents, sea state and local air-sea interactions are known  
260 to affect scatterometer measurements (Quilfen et al., 2001, 2004; Chelton and Xie, 2010; Kent et  
al., 2013; Bourassa et al., 2019; Mears et al., 2019) and contamination of satellite measurements  
262 by rain can still be a problem despite quality control and rain flagging. For the numerical model

winds, the surface winds from the 4-D model reanalysis are likely to be affected by several  
264 possible biases other than those that related to the calibration and editing of assimilated ocean  
surface wind data. As stated in Hersbach et al. (2018), erroneous climate signals can be  
266 introduced by the interaction between atmospheric numerical model bias and the evolving  
observing system, which remains a major concern in climate reanalysis. Any bias in the system  
268 can propagate and impact surface winds through the 4D variational analysis. As the oceans are  
relatively poorly instrumented with buoys, a recognized primary reference for surface wind data  
270 is provided by scatterometer instruments for which cross-calibration of different missions over  
time can be carefully performed. Belmonte and Stoffelen (2019) showed and discussed the biases  
272 of several  $\text{ms}^{-1}$  in the ERAI and ERA5 winds relative to ASCAT scatterometer, with a strong  
latitudinal dependence. However, they also showed that the ERA5 is a significant improvement  
274 over ERAI in this regard.

Another caveat regarding the use of these wind data sets for the study of coastal upwelling is the  
276 systematic data contamination by parasitic land effects due to the coarse resolution and poor  
land/sea transition profiles for the atmospheric model winds (Taboada et al., 2019; Belmonte and  
278 Stoffelen; 2019), and because the 25-50 km coastal blind zone for satellite winds makes gridded  
satellite winds (wind stress vector and curl) more sensitive to land contaminated ERAI nearshore  
280 winds. In this regard, and because CCMP also analyzes winds over land, CCMP coastal winds  
may be largely constrained and contaminated by over-land ERAI winds, especially during  
282 periods of scatterometer data gaps for which the blind zone of satellite data is approximately 50  
km.

284

286

### 288 **2.3 Chl-a and carbonate system data sets**

We are using two global reference datasets to assess trends in the California upwelling  
290 biogeochemical system. The Chl-a concentration is produced at a monthly and 4-km resolution  
by the Ocean Colour Climate Change Initiative project (OC-CCI, Jackson et al., 2019), covering  
292 the period 1998-2018. The surface partial pressure of carbon dioxide in seawater ( $p\text{CO}_2$ ) and  
seawater pH produced at a monthly and one-degree resolution is referenced as the Global Ocean  
294 Surface Carbon Product by the CMEMS project (Denvil-Sommer et al., 2019; Chau et al., 2020),  
and we used the 2020 version covering the period 1985-2018.  $p\text{CO}_2$  was estimated using a feed-  
296 forward neural network to reconstruct monthly values from a  $p\text{CO}_2$  climatology and input  
variables known to be the main physical, chemical and biological drivers: sea surface temperature  
298 and salinity, sea surface height, mixed layer depth, chlorophyll-a concentration, and the  
atmospheric  $\text{CO}_2$  mole fraction. The pH was calculated from  $p\text{CO}_2$  and the reconstructed surface  
300 ocean alkalinity whose time- and space-varying fields were obtained by a multivariate linear  
regression with salinity, temperature, dissolved silica and nitrate as independent variables.

302

### **3. Methods**

304 To evaluate upwelling intensity and its dependence on latitude, upwelling winds and derived  
Ekman transport were calculated for a series of twelve stations located every two degrees of  
306 latitude along the coast, approximately 100 km from the coast, which corresponds roughly to the  
boundary between the nearshore and offshore upwelling zones. These choices also avoids  
308 systematic contamination of data by parasitic land effects due to the coarse resolution and poor

land/sea transition profiles of numerical winds, and also due to the 25-50 km coastal blind zone  
310 for satellite winds that makes the gridded satellite winds (wind stress vector and curl) more  
sensitive to inaccurate nearshore ERAI wind data. Furthermore, the effective resolution of  
312 gridded satellite winds is no better than 100 km (Desbiolles et al., 2017), and even coarser for  
model winds, to make our choice of station locations appropriate. Figure 2 shows the location of  
314 the stations, with the seafloor elevation, and the mean annual Ekman transport and curl-driven  
velocity calculated using the CMEMS data. Table A1 in Appendix A provides specific  
316 information on stations location. The location of each station is chosen to correspond exactly to  
the latitude and longitude of a specific grid point in the CMEMS and CCMP grids, and the  
318 nearest ERA5 and ERAI grid points to the station coordinates were selected to avoid unnecessary  
interpolation. The selection of the nearest pixel in the grid does not introduce significant  
320 differences since the effective resolution is much coarser than the co-location distance. The same  
approach was applied to pH and pCO<sub>2</sub> data in that the selected pixel in the grid is that which is  
322 the closest to the coast. For Chl-a, we averaged the 4 km resolution data over an area of 50 (100)  
km square offshore (around) the location of coastal point (station ) to obtain the coastal and  
324 offshore values for Chl-a at each station. For coastal Chl-a, the coastal point is determined by the  
perpendicular distance between the coast and the intersecting the station.

326 Two main wind-driven processes determine the dynamics of EBUS, the coastal divergence of  
mass transport induced by the along-shore component of wind stress, defined as the cross-shore  
328 Ekman transport, and the vertical velocities associated with the wind stress curl, defined as the  
Ekman pumping/suction (e.g. Halpern, 2002; Capet et al., 2004). The first occurs at a cross-shore  
330 scale limited to a few tens of km from the coast (Estrade et al., 2008) while the second can extend

over a few hundreds of km. Both processes are quantified using solutions from Ekman's model

332 (Ekman, 1905) as follows:

334 1) The upwelling driven by the alongshore equatorward component of the wind stress,  
causing coastal divergence, is expressed by the cross-shore Ekman transport:

336 
$$\text{EKT} = \tau_{upw} / \rho f \quad (1)$$

where  $\tau_{upw}$  is the alongshore equatorward component of the wind stress. The unit of EKT  
338 is given in  $\text{m}^3\text{s}^{-1}$  per 100 m of coast length.

We also use a Cumulative Upwelling Index (CUI) that is calculated as the integration of the daily  
340 EKT along the Julian day of each year, and a Total Upwelling Magnitude Index (TUMI)  
calculated as the difference between the CUI values at the beginning and end of the upwelling  
342 season, as proposed in Bograd et al. (2009). To determine the beginning and end of the upwelling  
season, a 40-day Lanczos low-pass filter was first applied to the daily CUI records, and inflection  
344 points are searched for in prescribed time windows. This index accounts for the strong changes in  
the seasonality of the upwelling.

346

2) The upwelling caused by the wind stress curl is expressed by the vertical velocity at the  
348 base of the Ekman layer:

$$W = (\text{curl}\tau) / (\rho f) + (\beta\tau_x) / (\rho f^2) \quad (2)$$

350 where  $\text{curl}\tau$  is the wind stress curl,  $\rho=1.025 \text{ kg}\cdot\text{m}^{-3}$  is the air density,  $f=2\Omega\sin\phi$  is the Coriolis  
parameter,  $\Omega$  is the angular speed of the earth, and  $\phi$  is the latitude. The second term on the right  
352 side of the equation is a correction term for the  $\beta$  plane effect (derivative of  $f$  with latitude), and

$\tau_x$  is the zonal component of wind stress. The unit is usually given in  $\text{m s}^{-1}$ ,  $\text{cm day}^{-1}$ , or  $\text{m day}^{-1}$ .

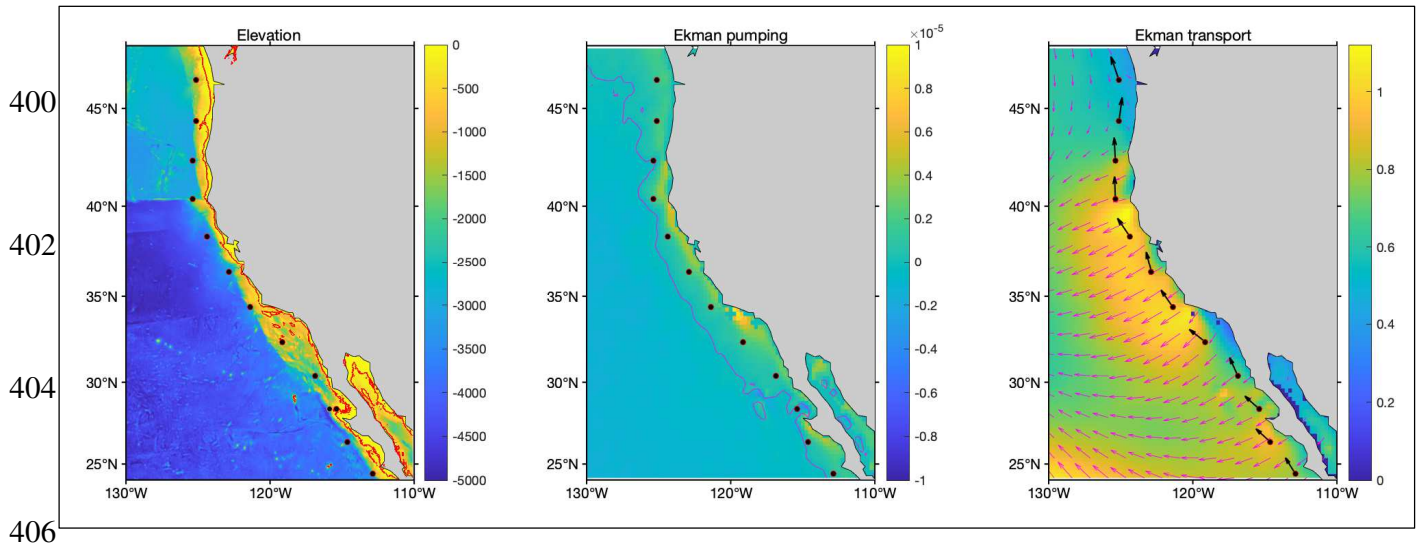
354 A positive upward (negative downward) value of  $W$  is called Ekman suction (pumping).

356 The water transport associated with the wind stress curl can be estimated as the integration of  $W$   
from coast to a given offshore location where the wind stress curl vanishes. In the CCUS, wind  
358 stress curl driven transport can be of the same order of magnitude as the Ekman transport EKT  
(e.g. Halpern, 2002; Pickett and Paduan, 2003). Wind stress curl is an ubiquitous feature in the  
360 CCUS due to the drop in wind stress at the coast, generated by the frictional retardation by land,  
and to wind disturbances usually observed in the lee of major headlands along the California  
362 coast (e.g., Cape Blanco, Cape Mendocino, Pt Arena, and Pt Conception), as shown in Figure 2,  
center panel.

364 Since there are no accurate long-term measurements of coastal winds over the entire CCUS to  
properly quantify these two upwelling processes, and given the relatively coarse effective spatial  
366 resolution of our wind data sets (no better than 100 km), we therefore monitor upwelling at the  
selected locations using EKT and  $W$  indices as first-order approximations or descriptions of the  
368 upwelling intensity, as was done in previous studies based solely on wind or surface pressure  
data. This implies some simplifications related to relevant upwelling dynamics as discussed in  
370 Estrade et al. (2008) and Marchesiello and Estrade (2010) which have shown that the upwelling  
intensity can be significantly limited by onshore geostrophic flow. Based on these results, Jacox  
372 et al. (2018) defined a new upwelling index for the California Current System, the Coastal  
Upwelling Transport Index (CUTI), which formally accounts for the geostrophic flow competing  
374 with the offshore Ekman transport. The geostrophic and Ekman transports are computed using  
the outputs of the high resolution Regional Ocean Modeling System (ROMS) with a surface wind

376 forcing that combines CCMP for the earliest period 1988-1998 and outputs from the high-  
resolution Coupled Ocean/Atmosphere Mesoscale Prediction System for the most recent period.  
378 This does not result in a single self-consistent reanalysis for our period 1996-2018 and we  
therefore did not include this recent upwelling indicator for our trend study, mostly because  
380 CCMP coastal winds are likely erroneous as discussed in section 2.2. However, Ding et al.  
(2021) showed that, in the context of global warming on long time scales, future changes in  
382 cross-shore geostrophic transport associated with changes in sea surface height along the  
California coast should certainly be better accounted for in upwelling trends analyses. Our  
384 approach using a first-order proxy for upwelling intensity at 100 km distance from the coast,  
where satellite data are not contaminated by land, can be further justified. Indeed, Jacox et al.  
386 (2014) showed that the mean upwelling transport and its trend, depicted using EKT indices based  
on CCMP winds, closely follow results obtained with the vertical transport over a 200 km wide  
388 coastal strip, calculated using ROMS vertical velocities. They showed, however, that this EKT  
proxy is biased high on average by ~ 25% in the central CCUS, an amount corresponding to the  
390 onshore geostrophic transport, and also showed that this is a more realistic estimate of upwelling  
intensity than the classical Bakun index (Bakun, 1973) based on the surface pressure fields of a  
392 low-resolution numerical model. Furthermore, it has also been shown for a recent period that  
long-term changes in upwelling intensity are related to changes in large-scale winds since there is  
394 a high temporal coherence along the coast between the Ekman pumping/suction and coastal  
divergence (Renault et al., 2015). For our analysis period, indices based on large-scale winds are  
396 therefore thought to be relevant for predicting the overall tendencies in coastal marine  
productivity (Renault et al., 2016; Turi et al., 2016).

398



400  
 402  
 404  
 406  
**Figure 2.** Location of the twelve stations (dots) and seafloor elevation (left, m), mean Ekman  
 408 vertical velocity (center,  $ms^{-1}$ , zero-contour as a magenta solid line), and mean Ekman transport  
 (right,  $m^2s^{-1}$ , black arrows indicate the orientation of the coastline used to derive  $\tau_{upw}$ )

410

In this paper, temporal trends are analyzed primarily using the most widely used non-parametric  
 412 Seasonal Mann-Kendall Trend Test (hereafter SKTT, Hirsch et al., 1982; Hirsch and Slack,  
 1984), and the associated Sen's slope estimate (Sen, 1968; Young and Ribal, 2019), which is a  
 414 randomness versus trend test that has been shown to be robust in comparison to parametric  
 alternatives for realistic stochastic processes (exhibiting seasonality, skewness and serial  
 416 correlation). Since perfectly linear trends rarely describe realistic evolution patterns of complex  
 meteorological processes, reducing the indication of possible monotonic trends given by SKTT to  
 418 that of a linear trend by the Sen's slope is certainly too restrictive and should be kept in mind.  
 The statistical significance of the estimated trends is tested and shown at  $p < 0.1$  in section 4 for a  
 420 graphical representation, and the p-values are given in section 5 when non-parametric and  
 parametric approaches are used. However, the interpretation of trend tests and associated p-

422 values should always be taken with caution and the following statement by Serinaldi et al.  
(2018), who discussed the issues related to trend tests at length, served as guideline in this study:  
424 “If a clear physical mechanism related to a predictable evolution of the properties of the process  
at hand is not identified, we cannot make conclusions about the reason of rejection or lack of  
426 rejection, since multiple factors not included in the null and alternative hypotheses can actually  
play a role”.

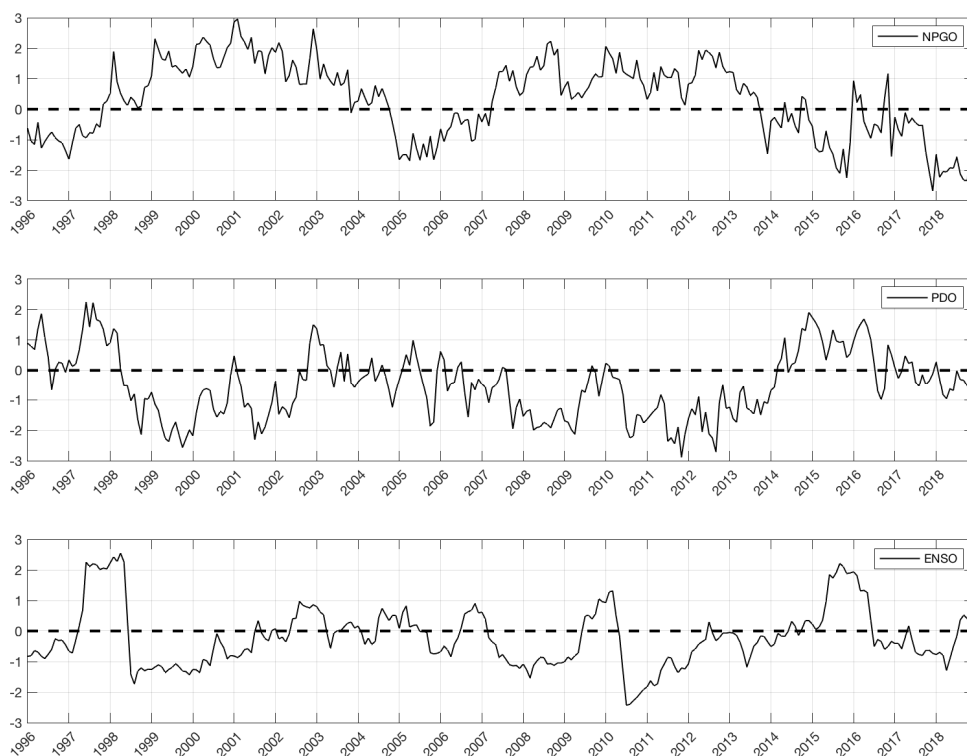
428

## 430 **4 Overall trends in the California Current Upwelling System**

### **4.1 Basin-scale climate variability**

432 The trends observed and discussed in the following sections should be placed in the context of  
natural basin-scale climate variability that imposes a remote forcing of the CCUS at interannual  
434 and near-decadal scales. Indeed, while studies predicting long-term changes in upwelling  
intensity (Bakun, 1990; Bakun et al., 2015; Rykacewski et al., 2015) have generated  
436 considerable interest in studying upwelling trends in the CCUS using historical data, as in  
Sydeman et al. (2014) for the period 1990-2012, such a period is certainly too short to obtain  
438 robust results on long-term changes associated with human activity, or it may simply be out of  
context if the forced changes emerge later in the 21<sup>st</sup> century (Brady et al., 2017). Three main  
440 interconnected climate signals exert remote control over the CCUS variability: the North Pacific  
Gyre Oscillation (NPGO), the Pacific Decadal Oscillation (PDO), and the El Niño-Southern  
442 Oscillation (ENSO), and this topic has been widely discussed in many studies (e.g. Di Lorenzo et  
al., 2008; Bograd et al., 2009; García-Reyes and Largier, 2012; Chenillat et al., 2012; Meinvielle  
444 and Johnson, 2013, Jacox et al., 2015; Kahru et al., 2018; Bonino et al., 2019). Figure 3 shows

that, for our analysis period 1996-2018, the PDO and ENSO are in a near neutral phase at the beginning and end of the period, while the NPGO is negative at both times. Overall, the NPGO and PDO show quasi-decadal variability, visibly anti-correlated, with abrupt phase changes for both indices (e.g. 1997/1998, 2004/2005, 2014/2015). The NPGO (PDO) is in average positive (negative) for the periods 1999/2003 and 2008/2013. The ENSO shows interannual variability with strong warm El-Niño events in 1997/1998 and 2015/2016, and weaker warm events in 2002 and 2010. At the beginning and end of our period, 1996-2018, there is no particular signature of these basin-scale climate signals that is likely to influence our trend analysis.



454 **Figure 3.** Monthly values of climate indices: top, North Pacific Gyre Oscillation (NPGO) index,  
 456 center, Pacific Decadal Oscillation (PDO) index, bottom, multivariate El Niño Southern  
 Oscillation (ENSO) index.

## 460 4.2 Observed trends in Chl-a, pCO<sub>2</sub>, and pH

Changes in the CCUS marine eco-system are subject to continuous monitoring and many studies  
462 involving in-situ measurements (e.g. Iles et al., 2012; Chan et al., 2017; Chavez et al., 2017) and  
numerical modelling of the coupled physical-biogeochemical ecosystem (e.g. Gruber et al., 2012;  
464 Hauri et al., 2013; Lachkar, 2014; Turi et al., 2016). But few global observational datasets are  
available to characterize its long-term evolution. Past efforts and recent developments have led to  
466 the provision of climatologies for some of the main biogeochemical parameters.

Figure 4 shows trends in Chl-a, pCO<sub>2</sub> and pH estimated from the high-resolution OC-CCI dataset  
468 for Chl-a and the lower-resolution CMEMS dataset for pCO<sub>2</sub> and pH, all of which are key  
variables in the marine ecosystem. Chl-a is used as a central metric of phytoplankton biomass and  
470 as a proxy for Net Primary Productivity (NPP), and pH is a key parameter for monitoring  
changes in the marine carbonate system with respect to ocean acidification. Annual mean Chl-a  
472 concentrations vary most strongly in the cross-shore direction, with a littoral ribbon of elevated  
Chl-a showing a seasonal cycle in opposite phase (Deutsch et al., 2020). Figure 4, left panel, thus  
474 shows the trends observed for the offshore and nearshore (< 50 km) areas of the CCUS. The  
trends (with  $p < 0.1$  intervals indicated) are observed nearshore with high latitudinal variability,  
476 showing an increase (decrease) in Chl-a concentration north (south) of 32°N during the period  
1998-2018. The observed trends in Chl-a and pH for the northern CCUS are comparable to those  
478 obtained in Turi et al. (2016) for the period 1997-2011, although their analysis did not cover the  
CCUS south of 30°N and therefore did not analyze the negative trends shown nearshore south of  
480 30°N in Figure 4. The central and bottom panels in Figure 4 show trends in pCO<sub>2</sub> and pH,

respectively, for the data pixel closest to the coast. At one-degree resolution, the CMEMS dataset  
482 does not clearly separate the nearshore area, whereas stronger trends are expected in the 100 km  
nearshore area (Turi et al., 2016). Trends are presented both for the full period covered by the  
484 dataset, 1985-2018, and for the 1998-2018 period covered by the Chl-a dataset. The positive  
(negative) trends in pCO<sub>2</sub> (pH) suggests that the carbonate system in the CCUS is subject to  
486 strong latitudinal variability, as for Chl-a, and to faster change for pH during the period 1998-  
2018. For this period, the largest decrease in pH, > 0.002 yr<sup>-1</sup>, is observed between 35°N and  
488 42°N (42° is the boundary latitude where downwelling conditions prevail on average). Turi et al.  
(2016) obtained comparable results from numerical modelling experiments, although they vary  
490 significantly with the forcing wind product, and suggested that the decrease in nearshore pH, and  
its latitudinal regionality, is mainly due to local increase in Dissolved Inorganic Carbon (DIC).  
492 Combined with the primary effect of increasing atmospheric CO<sub>2</sub> uptake, upwelling  
intensification is proving to be a robust driver for further increase in acidification and aragonite  
494 undersaturation in the CCUS (Lachkar, 2014; Chan et al., 2017), which is consistent with the  
pCO<sub>2</sub> and pH trend patterns in Figure 4. Changes in biological productivity are also strongly  
496 related to changes in intensity and timing of upwelling, but other geochemical and environmental  
factors are of primary importance, particularly nitrate concentration, and robust dome-shaped  
498 relationships between the different drivers have been identified (e.g. García-Reyes et al., 2014;  
Jacox et al., 2016). Therefore, the Chl-a trends presented in Figure 4 cannot simply be related to  
500 trends in upwelling winds.

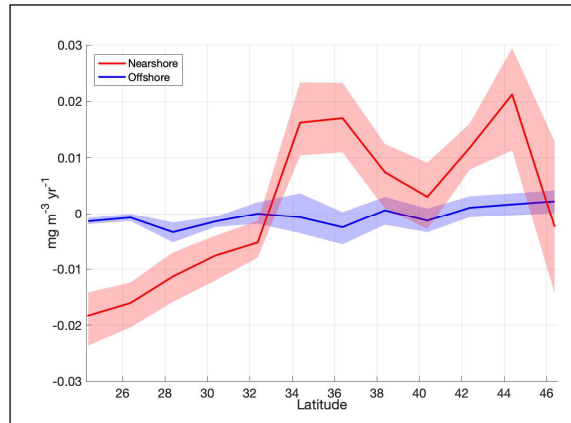
502

504

506

508

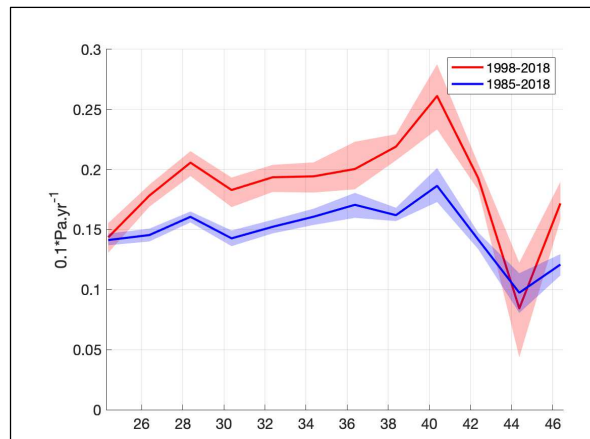
510



512

514

516



518

520

522

524

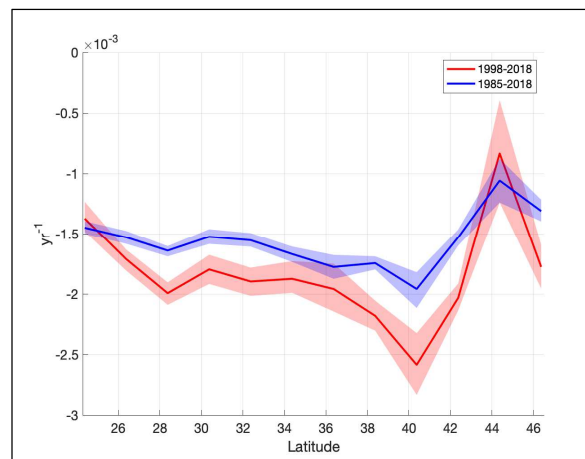


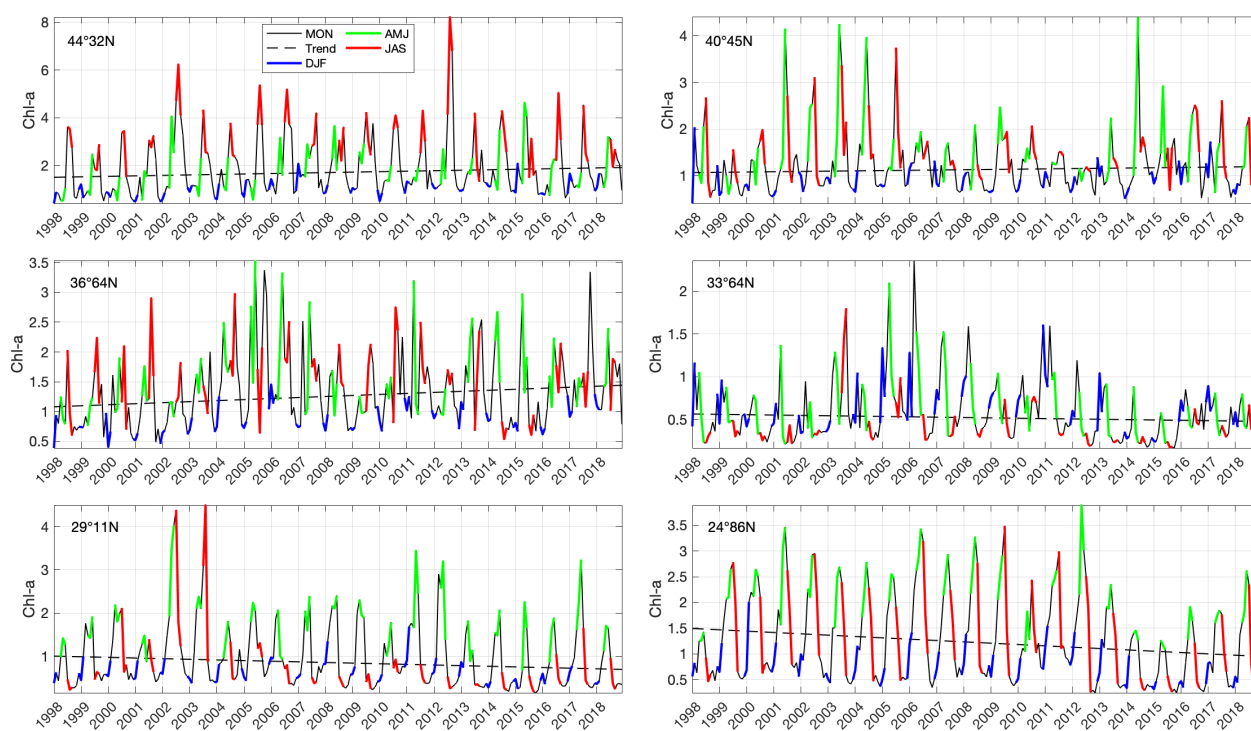
**Figure 4.** top panel: trends in Chl-a ( $\text{mg m}^{-3} \text{ yr}^{-1}$ ) nearshore (distance to coast  $< 50$  km, red solid line) and offshore ( $75$  km  $<$  distance to coast  $< 150$  km, blue solid line) for the period 1998-

2018. Central and bottom panels: trends in  $p\text{CO}_2$  (central panel,  $0.1\text{Pa yr}^{-1}$ ) and  $\text{pH}$  (bottom  
528 panel) for the periods 1998-2018 (red solid line) and 1985-2018 (blue solid line). The colored  
areas correspond to a  $p$ -value  $< 0.1$ .

530 To place the estimated trends in the context of the Pacific Ocean basin, examples of the high  
variability observed in the seasonal cycle of Chl-a are shown in Figure 5. Different reference  
532 seasons are defined as in García-Reyes and Largier (2012): the winter season (December-  
February), the upwelling season (April-June), and the relaxation season (July-September). The  
534 months of March, October and November are considered as transition periods. For Chl-a, there is  
overall little shift in seasonality in the northern and southern CCUS, with Chl-a values peaking  
536 during the upwelling or relaxation seasons depending on latitude, with some notable exceptions  
such as the much longer upwelling season in 2002 and 2003 near  $29^\circ\text{N}$  associated with much  
538 higher than usual Chl-a values, or in 2005 near  $40^\circ\text{N}$ . Conversely, there is a high variability in the  
central CCUS and Southern California Bight, where the peak of Chl-a occurs in almost all  
540 seasons. There is generally greater variability in maximum values than in minimum values at all  
locations and several noteworthy events can be related (Di Lorenzo et al., 2008) to the relative  
542 influence of the PDO, strong north of  $38^\circ\text{N}$ , the NPGO, strong south of  $38^\circ\text{N}$ , and ENSO. Thus,  
at  $40^\circ\text{N}$ , Chl-a is above average during the upwelling/transition seasons from 2001 to 2005 and  
544 below average from 1998 to 2001 and from 2006 to 2013, the latter periods corresponding to a  
positive phase of the PDO. Between  $37^\circ\text{N}$  and  $33^\circ\text{N}$ , the large positive anomalies in 2005 and  
546 2006 can be related to the remote forcing associated with a negative NPGO, although this was  
not observed in 2018 when NPGO was also strongly negative. Finally, the strong El Niño events  
548 of 1997/1998 and 2015/2016 and the marine heat wave, known as the “Blob event”, of 2014-  
2015 obviously strongly impact the Chl-a south of  $35^\circ\text{N}$ .

550 Kahru et al. (2018) correlated the variability of Chl-a during these warm events with the  
 frequency of SST, Chl-a fronts and the spring onset of upwelling. Jacox et al. (2016) also  
 552 analyzed several anomalous wind-driven events during the period 1998-2010 to describe the  
 optimal environmental conditions prevailing for biological productivity, and to define a  
 554 framework for the bottom-up control of the productivity by the wind stress and nitrate  
 concentration drivers. They showed that basin-scale remote forcing and changes in the upwelling  
 556 season timing are of primary importance.

In the following sections, we therefore focus on trends in upwelling winds and changes in  
 558 upwelling phenology that may result from basin-scale remote forcing or long-term wind changes,  
 and that impact the CCUS biogeochemical ecosystem.



560 **Figure 5.** Monthly values of coastal Chl-a ( $\text{mg m}^{-3}$ , averaged over a distance to coast < 50 km)  
 562 for the periods 1998-2018, and seasonal values such as: December/January/February (DJF,

blue line), April/May/June (AMJ, green line), July/August/September (JAS, red line).  
564 March/October/November (MON, black line). The dashed black lines show the trend as estimated  
in Figure 4. The latitude shown in the upper left corner of each plot is the latitude of the coastal  
566 point located on the perpendicular to stations 1, 3, 5, 7, 9, 11 from bottom-right to top-left (see  
Table A1 for details).

568

### 4.3 Observed trends in upwelling winds

570 Although the main driver of ocean acidification is the accumulation of anthropogenic CO<sub>2</sub> from  
the atmosphere, climate fluctuations can enhance or mitigate this acidification trend within the  
572 EBUS, and the assessment of this trend is therefore highly dependent on the choice of start and  
end years for the time record being analyzed. For example, a strong El Niño signal prevailed  
574 during the winter of 1997-1998 (see Figure 3), which is associated with stronger southerly winds  
during winter in the northern CCUS, a delayed upwelling season, and a reduction in equatorward  
576 upwelling-favorable winds in central and northern CCUS (Jacox, 2014; Turi et al., 2016). Other  
human-induced changes are predicted, including an increased contrast between atmospheric  
578 pressure over the ocean and land, leading to an increase in upwelling winds (Bakun, 1990), or,  
more recently, a long-term poleward shift of ocean high pressure systems, leading to a long-term  
580 increase (decrease) in summer upwelling-favorable winds in the northern (southern) CCUS  
(Bakun et al., 2015; Rykaczewski et al., 2015), both of which are likely to contribute to changes  
582 in the carbon system.

The objective of this work is thus to link this observed large-scale trend in biogeochemical  
584 parameters, and its latitudinal structuring, to atmospheric forcing. To do so, and as indicated in  
the data section, the approach chosen is based on the use of different state-of-the-art wind data

586 sources and on an appropriate choice of the beginning and end of the analyzed period in order to  
ensure a good coverage by satellite winds while minimizing effects of the main climate signals.

588 Average alongshore winds are favorable for upwelling, except north of 44°N where downwelling  
conditions prevail slightly on average at our two northernmost stations, as shown on the average  
590 Ekman transport chart (Figure 2, right panel). For greater clarity, the trends estimated using the  
SKTT over the period 1996-2018 and the associated  $p < 0.1$  confidence limits are presented  
592 separately in Figure 6 for the numerical models winds (left panels) and for the analyzed satellite  
winds (right panels). The upper panels show the estimated annual trends at each station, using the  
594 SKTT and monthly time series over all seasons. This is computed as the median value of the  
trend obtained using Sen's regression applied to each of the twelve months concurrently to  
596 estimate a single trend. Thus, this SKTT configuration is specifically designed to provide a  
single summary statistic for the entire record and will not indicate when there are differing trends  
598 in different months or seasons. To study trend seasonal dependence, the bottom panels therefore  
show independently estimated seasonal trends for the three characteristic seasons defined in  
600 section 4.2. Overall, from the upper panels, a very similar behavior is obtained for CCMP and  
CMEMS satellite winds, showing stronger upwelling-favorable winds between 34°N and 42°N,  
602 an area located approximately between Point Conception and Cape Blanco. The model winds  
also show a similar trend at these locations, but with lower levels of significance, and show a  
604 trend towards reduced upwelling winds in the southern part of the CCUS that is not observable in  
the satellite data.

606 The seasonal analysis shows, in lower panels of Figure 6, a better agreement between the model  
reanalysis products and the satellite analysis products for the winter season for which upwelling-  
608 favorable trends of comparable magnitudes are found between 35°N and 45°N. South of 33°N,

weaker trends of reduced upwelling winds are found with  $p < 0.1$  for ERA5, ERAI, and CMEMS  
610 at different locations. For the upwelling season, comparable upwelling-favorable trends are also  
found between about  $38^{\circ}\text{N}$  and  $43^{\circ}\text{N}$  with satellite and model reanalysis products, but with  
612 different levels of significance. South of  $33^{\circ}\text{N}$ , trends towards reduced upwelling winds ( $p < 0.1$ )  
are found with ERA5. For the transition season, no trend at  $p < 0.1$  is observed with the satellite  
614 products, while trends towards reduced upwelling winds with  $p < 0.1$  are observed with ERA5  
and ERAI at several locations in the southern zone. In summary, trends of stronger upwelling  
616 winds are consistently found during the winter and upwelling seasons, between about  $35^{\circ}\text{N}$  and  
 $45^{\circ}\text{N}$ , and equivocal results are found in the southern zone, with trends of reduced upwelling  
618 winds being only identified within the model reanalysis products. This difference in trends is  
reflected in the evolution over time of the comparison statistics between the models and the  
620 satellite winds (Figure 1). Indeed, for the ERA5 alongshore winds at southern stations (1 to 4),  
the high bias with the CCMP was significantly reduced between the first and second half of the  
622 analysis period. For the ERAI and stations 4 to 7 between  $30^{\circ}\text{N}$  and  $36^{\circ}\text{N}$ , the low bias with the  
CCMP increased. However, these observed differences are consistent with results presented in  
624 Belmonte and Stoffelen (2019) in which the weaknesses of the ERA5 and ERAI are discussed at  
global and local scales. They further show that the ERA5 is however a significant improvement  
626 over the ERAI.

628

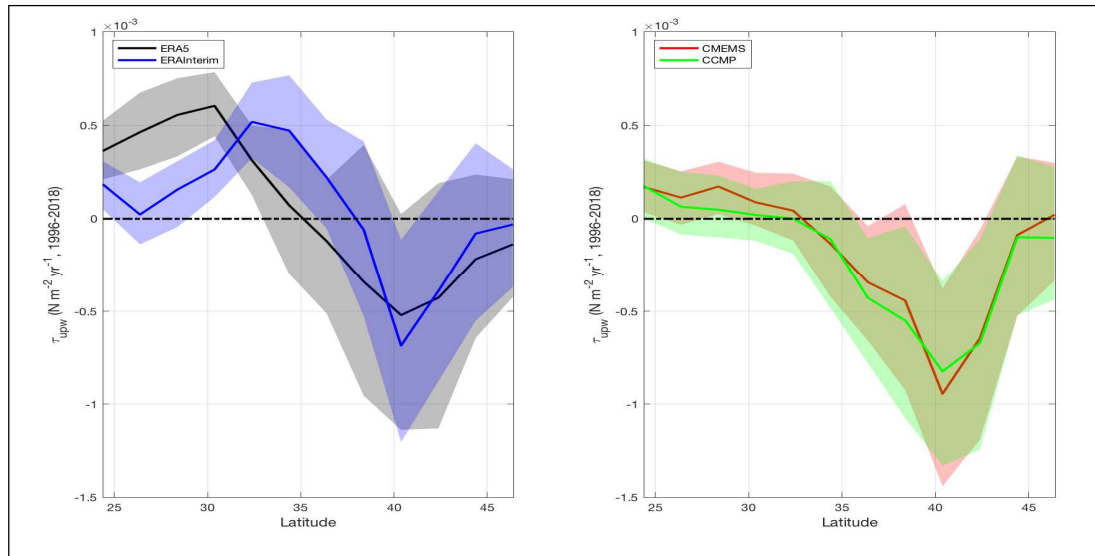
630

632

634

636

638

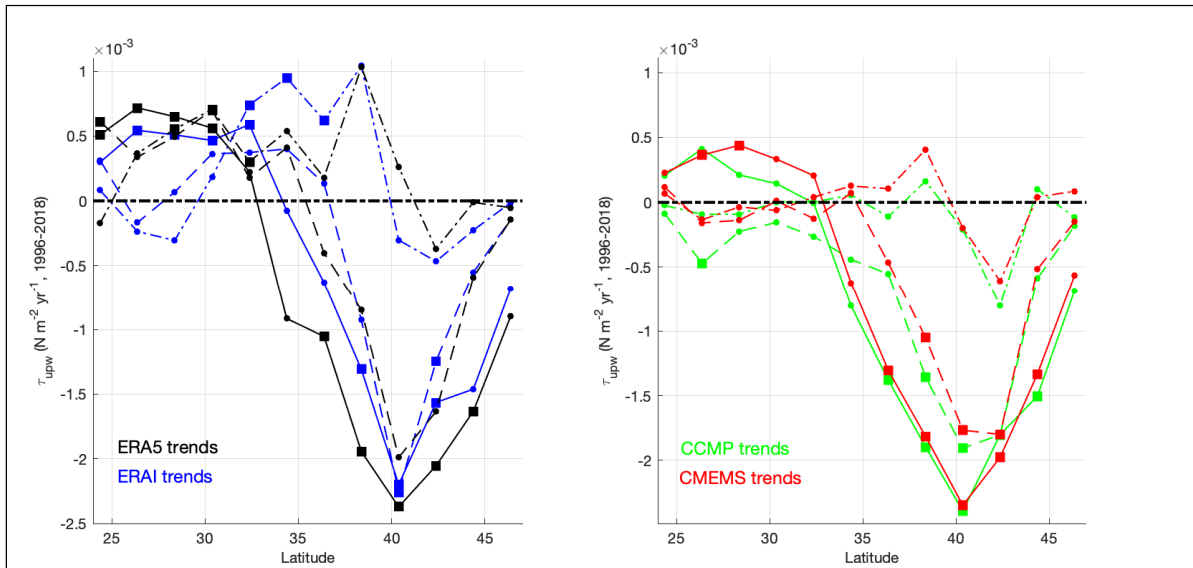


640

642

644

646

648 **Figure 6.** Top panels: Annual  $\tau_{upw}$  trends ( $N \cdot m^{-2}$  per year, negative for increasing equatorward

650 winds) as a function of latitude, for the twelve stations, over the period 1996-2018, for model

651 winds (left panel) and satellite winds (right panel). The color-shaded areas correspond to p-value

652  $< 0.1$ . Bottom panels: Seasonal  $\tau_{upw}$  trends ( $N \cdot m^{-2}$  per year) over the same period and on the

653 same x-axis for model winds (left panel) and satellite winds (right panel), for the winter season

654 (solid lines), the upwelling season (dashed lines), and the transition season (dashed-dotted lines).

654 Filled squares indicate  $p < 0.1$ . The color code follows ERA5 in black, ERAI in blue, CMEMS in  
655 red, CCMP in green.

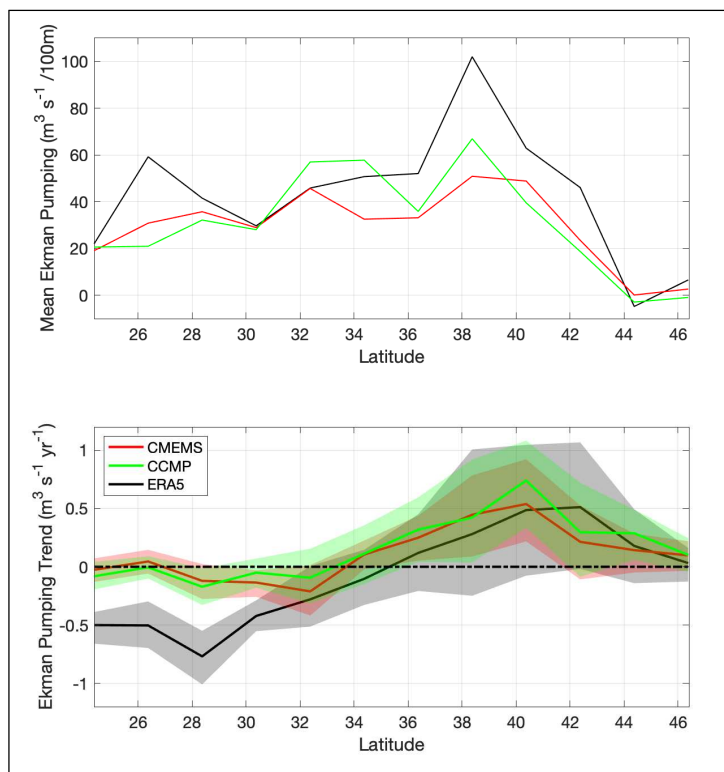
656 Alongshore wind stress is the main driver for coastal upwelling, but the wind stress curl caused  
657 by the wind slackening at coast or by reduced intensity downwind of headlands (i.e. a wind  
658 shadowing) is another important source of vertical velocities. In Figure 7, the mean annual curl-  
659 driven transport, integrated from the coast to each station, is presented for only three of the data  
660 sources because the ERAI resolution does not allow for such integration. This shows that  
661 upwelling conditions prevail on average south of  $44^{\circ}\text{N}$ , with significant differences between the  
662 satellite-derived and ERA5 transports. These can be related to the systematic differences in wind  
663 stress curl already shown in Belmonte and Stoffelen (2019). The curl-driven velocities and  
664 associated transport show the same trend structuring as for the alongshore winds in Figure 6, with  
665 a comparable level of uncertainty, which is the result, on average, of the strong correlation  
666 between the increase (decrease) of offshore winds and the increase (decrease) of the wind stress  
667 curl. So overall, the results of trend analysis using satellite and model analyses are contradictory  
668 in the southern part of the CCUS.

670

672

674

676



678 **Figure 7.** Top panel: average integrated Ekman pumping transport ( $m^3s^{-1}$  per 100m of coast) as  
a function of latitude, for the twelve stations, averaged over the 1996-2018 period. Lower panel:  
680 associated trends ( $m^3s^{-1}$  per year) over the same period and same x-axis for ERA5 in black,  
CMEMS in red, CCMP in green.

682

The spatial structuring of the trends observed in our study can be related to the trends obtained  
684 for the biogeochemical parameters in Figure 4. Increased upwelling favorable winds are  
associated with increased Chl-a concentrations, decreased pH and increased  $pCO_2$  between  $36^\circ N$   
686 and  $42^\circ N$ . South of  $34^\circ N$ , results obtained with the different wind datasets diverge.

In the next section, we analyze in-depth changes in the CCUS phenology associated with large-  
688 scale climate fluctuations, in order to better identify the possible long-term trends in CCUS  
intensity associated with the trend in upwelling winds that have been consistently found in this  
690 section.

## 692 **5. Changes in the upwelling phenology**

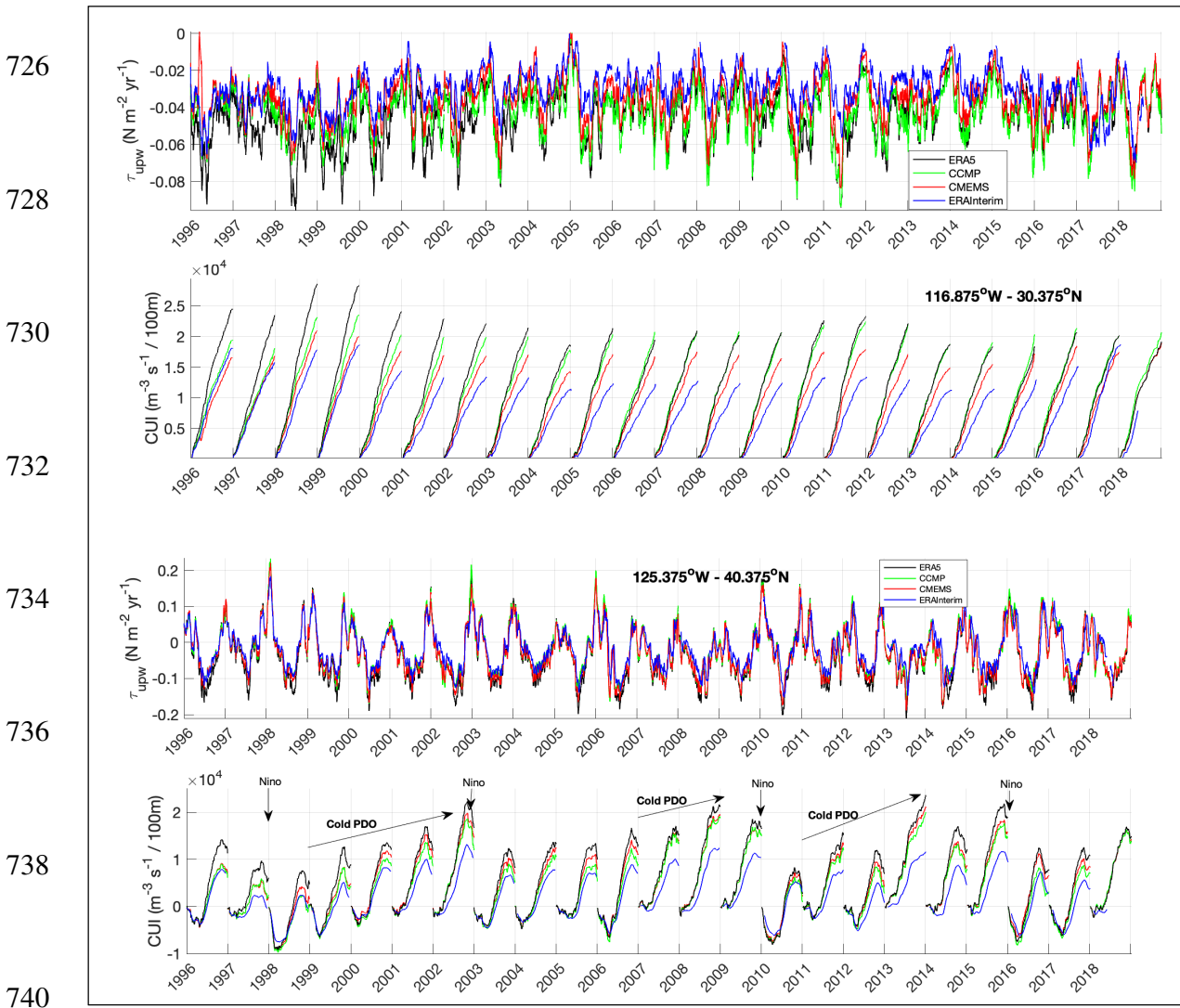
The marine ecosystem of the EBUS is largely influenced by the seasonality of upwelling winds  
694 and more specifically by the phase and intensity of upwelling favorable winds, i.e. the phenology  
of upwelling. Indeed, large scale climate signals modulate the seasonality of the CCUS and the  
696 key climate signals discussed in section 4.1 are correlated with changes in the phenology of the  
CCUS (e.g. Di Lorenzo et al., 2008; Bograd et al., 2009; García-Reyes and Largier, 2012;  
698 Chenillat et al., 2012; Meinvielle and Johnson, 2013, Bonino et al., 2019).

Bograd et al. (2009) analyzed these influences by mapping of a cumulative upwelling indice,  
700 CUI, and other within-season indices. The CUI is computed as the integration of the daily cross-  
shore Ekman transport along the Julian day of each year. Since upwelling winds have a  
702 cumulative effect on ecosystem productivity through the provision of nutrient-rich waters, the  
CUI itself can provide useful information on changes in ecosystem productivity, although it is  
704 only one of the primary factors relating to net primary production and linked to nutrient supply  
(García-Reyes et al., 2014; Jacox et al., 2016). Here we seek to analyze long-term changes in the  
706 seasonality of upwelling for two of the stations where the wind trends were consistently found at  
 $p < 0.1$  (Figure 6). Figure 8 shows the upwelling winds and associated CUI at  $30^{\circ}375$  N and  
708  $40.375^{\circ}$  N, where a trend towards less favorable upwelling winds was found with ERA5 and  
ERA1 at the southern location, and a trend towards stronger upwelling winds was found with  
710 CCMP and CMEMS at the northern location.

The upper panels show, for  $30^{\circ}375$  N, the large difference between the ERA5 alongshore winds  
712 and the satellite winds at the beginning of the period, as discussed in the previous sections, with  
the ERA5 CUI being significantly larger than other CUIs until about 2002. At  $30^{\circ}375$ N, the CUI  
714 increases continuously each year, indicating almost constant equatorward winds, with a clear  
decadal modulation in the maximum of the CUI. For all data sources, the CUI tends to be higher  
716 for the negative (positive) phases of the PDO (NPGO) and also higher for some of the strong La  
Niña conditions that followed El Niño events such as in 1998-1999 and 2010-2011.

718 At  $40^{\circ}375$ N, the interannual variability is strikingly illustrated by the annual mapping of CUI and  
the signatures of the ENSO and PDO are clear. In central and northern CCUS, El Niño years are  
720 associated with stronger southerly winds in winter, leading to minima in CUI which appear to be  
related to the strength of ENSO, as in 1997/1998, 2009/2010, and 2015/2016. Typically, El Niño

722 years are followed by cold phases of the PDO during which the northerly winds are weaker in  
 723 winter, the upwelling season begins earlier and the maximum CUI increases until another  
 724 positive ENSO occurs.



742 **Figure 8.** Mean alongshore upwelling winds ( $\tau_{upw}$ ,  $N.m^{-2}$ , negative when equatorward) and  
 743 associated CUI ( $m^{-3}.s^{-1} / 100m$ ) as a function of time, at 116°875W – 30°375N (top panels) and  
 744 125°375W – 40°375N (bottom panels). The color code follows ERA5 in black, CMEMS in red,  
 745 CCMP in green, ERAInterim in blue.

746 These significant changes in CCUS phenology associated with large-scale climate signals make it  
difficult to detect long-term trends in upwelling forcing, although 1996 and 2018 can be  
748 considered relatively neutral years in this regard. Therefore, to investigate this issue further, we  
use the Total Upwelling Magnitude Index (TUMI, see the Methods section) calculated as the  
750 difference between the CUI values at the beginning and end of the actual upwelling season, as  
proposed by Bograd et al. (2009). This index takes into account the large variations in the  
752 upwelling seasonality and therefore better represents the actual cumulative effect of upwelling on  
ecosystem productivity than a conventional integration of upwelling winds over a fixed  
754 upwelling season (usually April to June or July). In addition, this index was also tested by  
integrating only over upwelling favorable daily transports during the actual upwelling season;  
756 this had no significant impact on the following results. The first two panels in Figure 9 show, for  
the four sources of wind data, the TUMI as a function of the year at the two stations analyzed in  
758 Figure 8. The two lower panels show the detected duration and start time of the upwelling season  
at 40.375°N only, since the upwelling season is almost year-round at 30°375° (Figure 8, panel b).  
760 At 40°375N, it shows almost perfect agreement between the data sources for season length and  
start time, with no clear temporal trend but with a large interannual variability. Values of up to 3  
762 and 5 months year to year difference for start and duration, respectively, which can be related to  
the combined influence of large scale climate signals. Good agreement between wind products is  
764 found for TUMI at 40.375°N although the CCMP is significantly lower, with a near-decadal  
modulation showing an increase in TUMI during the negative phase of the PDO associated with  
766 high TUMI maxima in 2002, 2008 and 2013. There is a clear positive trend, which is assessed  
using the non-parametric SKTT method and the Matlab parametric “robustfit” function. The

768 latter performs an iterative least-squares regression to a linear model by iteratively changing the  
model coefficients to limit the influence of the data points farthest from the linear model. For  
770 example, the “robustfit” linear regression gives less weight than a simple linear regression to the  
1998/1999 TUMI data strongly affected by the 1998/1999 La Niña event (Figure 9, top panel).  
772 The use of “robustfit” gives a significant increase in TUMI between 1996 and 2018 of +27.2%  
( $p=0.0655$ ), +24.0% ( $p=0.0943$ ), +15.2% ( $p=0.1786$ ), and +13.1% ( $p=0.2466$ ) for CCMP,  
774 CMEMS, ERAI and ERA5, respectively. The use of SKTT gives +34.1% ( $p=0.039$ ); +28.9%  
( $p=0.051$ ); +10.2% ( $p=0.342$ ); +15.4% ( $p=0.09$ ) for CCMP, CMEMS, ERAI and ERA5,  
776 respectively. Estimated trends with  $p < 0.1$  are found only for CCMP and CMEMS, and these  
results are consistent with those obtained in section 4 although, not surprisingly,  $p$ -values vary.  
778 At  $30^{\circ}375N$ , there are large differences in mean TUMI values, with CMEMS and ERAI being  
significantly lower, and the intriguing temporal evolution of the ERA5 data is again clearly  
780 indicated by much higher TUMI values at the beginning of the period. Although it does not vary  
as much as observed at  $40^{\circ}375N$ , due to the lack of strong seasonality, the low-frequency  
782 modulation shows periods of high TUMI, in 1998-1999 and 2010-2012, associated with negative  
phases of the PDO and ENSO. Over the period 1996-2018, the “robustfit” analysis gives a  
784 positive trend of +5.4% ( $p=0.3384$ ), +5.7% ( $p=0.1728$ ), and a negative trend of -29.5% ( $p=$   
 $0.0041$ ) and -22.9% ( $p=0.0013$ ) for CCMP, CMEMS, ERAI and ERA5, respectively. Using  
786 SKTT one obtains +3.1% ( $p=0.398$ ); +1.3% ( $p=0.792$ ); -21.6% ( $p=0.035$ ); -26.2% ( $p=0.001$ ) for  
CCMP, CMEMS, ERAI and ERA5, respectively. Only the estimated trends for ERAI and ERA5  
788 exhibit a  $p < 0.1$ , which is consistent with the results of section 4. But it is still unexplained why  
the variability patterns in ERA5 are so different there, as well as the rapid increase in ERAI  
790 TUMI at the end of the period.

792

794

796

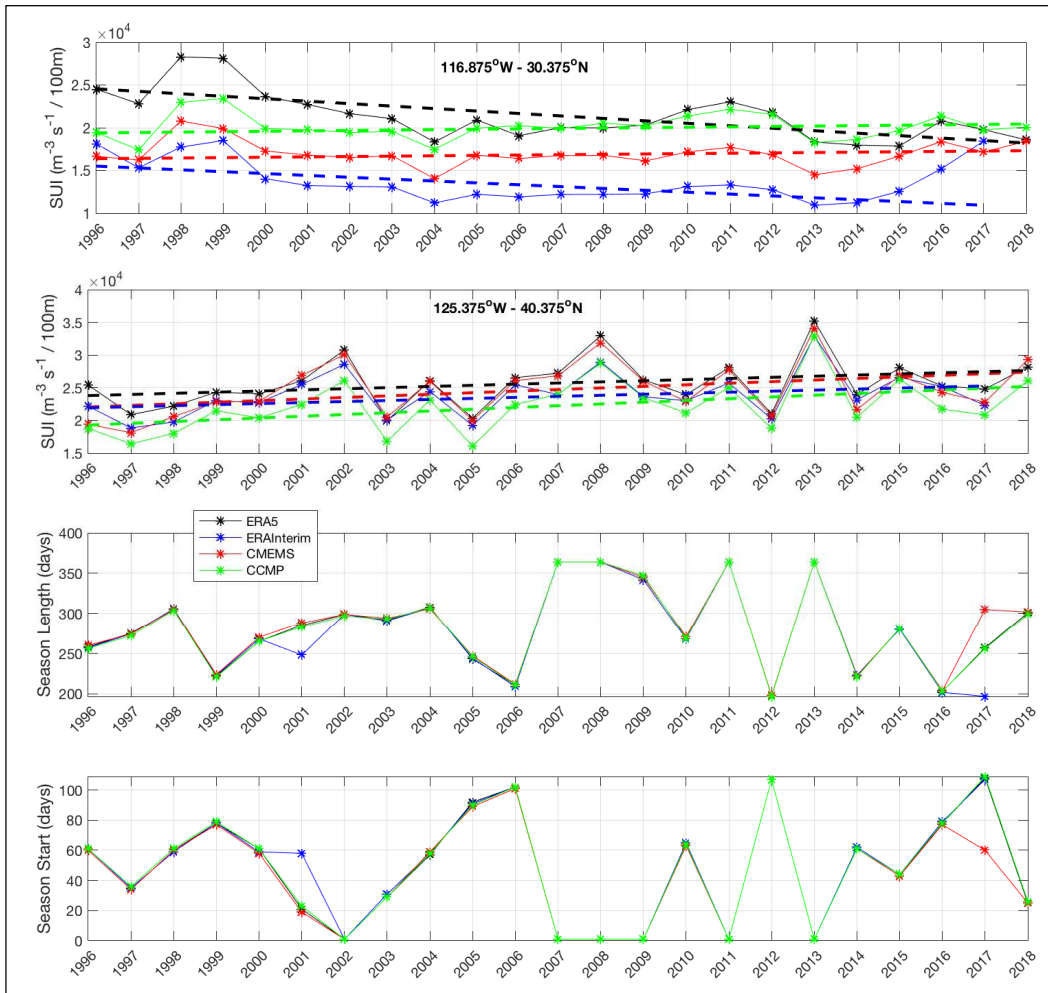
798

800

802

804

806



808 **Figure 9.** Total Upwelling Magnitude Index (TUMI,  $\text{m}^3 \cdot \text{s}^{-1}$  per 100m) as a function of time at  
810  $116^\circ 875\text{W} - 30^\circ 375\text{N}$ , first top panel, and  $125^\circ 375\text{W} - 40^\circ 375\text{N}$ , second top panel. For  
812  $125^\circ 375\text{W} - 40.375^\circ\text{N}$  the associated upwelling season length (number of days, first lower  
panel), and day of upwelling season start in each year (second lower panel). Dashed lines in top  
panels show the trends obtained with the SKTT method. The color code follows ERA5 in black,  
ERAInterim in blue, CMEMS in red, CCMP in green.

814

## 816 **6. Discussion and summary**

Long-term trends have been predicted in the four eastern boundary upwelling systems that are  
818 related to anthropogenic, deterministic and predictable changes in large-scale atmospheric  
pressure systems (Bakun, 1990; Bakun, 2015; Rykacewski et al., 2015). In this work, we have  
820 examined the case of the California Current Upwelling System for the recent time period and  
have paid particular attention to the issue of data.

822

### **6.1 Surface wind data issues**

824 Our approach is based on the use of surface winds from recent and mostly used model re-  
analyses (ERA-Interim and ERA5) and satellite analyses (CCMP and CMEMS), over a period for which  
826 scatterometer wind vectors provide a reliable spatially-resolved dataset (speed and direction) and  
for which no large trends are observed in the most important climate signals in the Pacific Ocean.  
828 Therefore, although the 1996-2018 analysis period is relatively short with respect to natural near-  
decadal climate variability, a robust analysis of temporal trend can still provide reliable  
830 information on changes in upwelling winds over this period. Although the length of data records  
has been an obvious problem addressed in most studies of upwelling trends, a much overlooked  
832 issue is the long-term temporal consistency of the most widely used wind data sets.

In this regard, the use in our study of several different data sets with a discussion of their  
834 respective potential weaknesses is a necessary step. None of these data sets can be considered  
independent of the others, and each of them is likely to have uncharacterized biases that can be  
836 misinterpreted as geophysical trends. Indeed, although each of the wind products used in the

study was developed with the objective of ensuring temporal consistency, this consistency is  
838 poorly documented and therefore possibly unverified regionally. With respect to satellite data, the  
development of climate data records for each instrument is a recent concern and it can be  
840 therefore be difficult for multi-satellite gridded products to achieve the accuracy required for  
climate studies (Bourassa et al., 2019). This may be due to problems related to the evolution of  
842 the observing systems and to the difficulty to cross-calibrate the various instruments. But also  
due to the fact that the two main multi-satellite winds products (CCMP and CMEMS) both make  
844 use of ERAI model winds to ensure consistency of analysis in satellite data gaps. The relative  
influence of ERAI winds in CMEMS products was extensively discussed in Desbiolles et al.  
846 (2017), using sensitivity experiments to various input data, and validation using independent  
buoy and scatterometer data. They show a significant improvement in validation statistics for  
848 CMEMS winds compared to ERAI winds, but they also conclude that the use of ERAI winds in  
CMEMS products may remain an obvious drawback. This supports our choice of a period for  
850 which scatterometer data are available with good enough coverage to limit the influence of ERAI  
winds. For the numerical model winds, the surface winds from the 4-D model reanalysis are  
852 likely to be affected by several possible biases other than that related to the calibration and  
editing of assimilated ocean surface wind data. As stated in Hersbach et al. (2018), spurious  
854 climate signals can be introduced from interaction between atmospheric numerical model bias  
and the evolving observing system which remains a major concern in climate reanalysis. Any  
856 bias in the system can propagate and affect surface winds through the 4D variational analysis. For  
example, Belmonte and Stoffelen (2019) showed systematic biases of several  $\text{ms}^{-1}$  in the ERAI  
858 and ERA5 winds relative to the ASCAT scatterometer observations, with a strong dependence on  
latitude. Analyzing several atmospheric re-analyses, including the ERAI, with the CCMP as a

860 baseline for comparison, Taboada et al. (2019) showed similar results and concluded with a  
recommendation of testing the sensitivity of derived results to the choice of wind product. This is  
862 what we have done to analyze trends in the CCUS, using the latest ERA5 and CMEMS products  
to help better mitigate the various data issues discussed in this section. Indeed, the ERA5 re-  
864 analysis is the ERAI follow-on and shows a great improvement over the latter data set at global  
and local scale (Hersbach et al., 2018; Hersbach et al., 2020; Belmonte and Stoffelen, 2019).  
866 Although we also show this significant improvement with the most recent re-analysis, large  
systematic, latitude-dependent biases between numerical and satellite upwelling winds still  
868 remain. ERA5 has generally larger upwelling wind magnitude and variability than CCMP and  
CMEMS during the first half of the period and closer statistics during the second half. The  
870 significant decrease in ERA5 upwelling winds over the period in the southern CCUS is not  
observed in satellite winds, which remains unexplained, indicating that large uncertainties, at the  
872 regional or global scale, can still remain in the most recent wind data sets (i.e. both model re-  
analyses and from satellites). The CMEMS data set shares many similar characteristics with the  
874 CCMP, but it has also different characteristics of interest for our analysis: 1) it does not use the  
buoy data which is done to allow independent assessment with these reference in-situ winds, and  
876 to avoid artifacts in the calculation of wind stress curl at locations close to buoys (Mears et al.,  
2019); 2) it is less dependent on ERAI numerical winds for our analysis period and in near-  
878 coastal areas because it uses a longer scatterometer data record and because it is not as  
constrained by ERAI winds over land as the CCMP is. Indeed, near the coast, the 25-50 km blind  
880 zone for satellite winds makes the CCMP winds (wind stress vector and curl) more strongly  
influenced by ERAI land winds, since CCMP also calculates winds over land. In coastal regions,  
882 the contamination of numerical model winds with lower winds over land and the coarse

representation of the ocean-land transition in atmospheric reanalyses indeed degrade the ability to  
884 reproduce realistic upwelling patterns. In the methodological approach chosen for this study, we  
therefore do not use the wind data for the grid pixels closest to the coast so that our results are  
886 less affected by these problems. Interestingly, at the offshore stations we have selected, we found  
a remarkable agreement between CCMP and CMEMS upwelling winds and estimated trends.  
888 This may imply increased robustness in our results derived from wind analyses that are tailored  
to satellite observations.

890

## **6. 2 Observed trends in upwelling wind forcing and ecosystem response**

892 As we have consistently found for key biogeochemical system parameters (i.e. Chl-a, pCO<sub>2</sub> and  
pH in our study) a spatially structured pattern of trends is observed in upwelling winds and  
894 associated Ekman transport with the four wind data sources, with trends towards more favorable  
upwelling winds in the CCUS core (approximately between Point Conception to Cape Blanco,  
896 35°-43° latitude). This trend is verified with  $p < 0.1$  in the annual data only for the CCMP and  
CMEMS satellite analyses. By defining seasons following the methods of García-Reyes and  
898 Largier (2012), seasonal trends of greater amplitude than the annual trend are identified, with  $p <$   
0.1, with a comparable amplitude for model reanalysis and satellite analysis products in the  
900 winter (December-February) and upwelling (April-June) seasons. The relaxation season, from  
July to September, does not show such a trend towards increased upwelling winds. Ambiguous  
902 results are found in the southern CCUS with negative trends found ( $p < 0.1$ ) for the model  
reanalysis products but not from the satellite products. This difference in trends is the result of  
904 the temporal evolution of geographically distributed average biases between the satellite analysis  
and the model reanalysis products, which remain unresolved.

906 The strong spatial structuring of the observed trends for the biogeochemical parameters, pCO<sub>2</sub>,  
pH and Chl-a is consistent with long-term changes in upwelling modulating the carbonate  
908 system, as discussed in Turi et al. (2016). Our results showing spatial structuring in the long-term  
trends of upwelling winds may explain the similar structuring observed in the increase in  
910 nearshore pCO<sub>2</sub> and Chl-a and decrease in pH, north of 34°N in the core of vthe CCUS.  
However, the precise relationships between the biogeochemical system of the CCUS and local or  
912 remote forcing can certainly be better analyzed by approaches that combine eddy-resolving  
regional models with various hydrographic and remote sensing observations (e.g. Jacox et al.,  
914 2016; Deutsch et al., 2020).

Previous studies devoted to the variability of the CCUS (e.g. García-Reyes and Largier, 2012;  
916 Sydeman et al., 2014) defined the upwelling season in a fixed time window, which raises the  
question of taking into account the large changes that occur in the upwelling phenology under  
918 natural climate forcing. Our results also show the large differences that occur in the timing of the  
upwelling season in response to the relative influence of the ENSO, NGPO and PDO, and this is  
920 consistent with previous studies (e.g. Di Lorenzo et al., 2008; Bograd et al., 2009; García-Reyes  
and Largier, 2012; Meinvielle and Johnson, 2013). The Cumulative Upwelling Index, CUI, is  
922 used to define the start and end times of the upwelling season and an associated seasonal  
upwelling index, the TUMI, represents the integration of the Ekman transport along the actual  
924 upwelling season. Variations in TUMI are better related to actual ocean productivity than an  
index calculated over a fixed time window to define the upwelling season. Changes in the timing  
926 of the upwelling season are remarkably consistent for satellite analyses and model re-analyses,  
but mean values of the TUMI vary significantly due to the observed differences in the mean  
928 along-shore wind stress between the different products. ERA5 TUMI values are significantly

higher at the beginning of the period, resulting in differences in estimated trends. As observed  
930 throughout this study, there is remarkable agreement between the results obtained with the two  
satellite analysis data sets.

932 Remarkably, the satellite product results show that TUMI has increased by 25% or more in the  
central CCUS, whereas the model reanalyses give an increase of 15% or less. In the southern  
934 CCUS, TUMI trends are negligible with satellite products, whereas a decrease in TUMI of 20%  
or more is achieved locally with model reanalysis products.

936

### **6.3 Summary**

938 Long-term changes in the marine ecosystems of the EBUS are predicted due to anthropogenic  
climate change. In particular, global ocean acidification is having a profound effect on the coastal  
940 waters of the EBUS, affecting the entire trophic chain, net primary production and related  
economic activities such as fisheries. Another predicted change related to human activity is that  
942 of upwelling dynamics with expected long-term changes in upwelling winds, which raises the  
interest in monitoring upwelling using validated, self-consistent wind data sets. Indeed, the  
944 results of past trend analyses using historical wind data show a high degree of uncertainty  
depending on the EBUS considered, the effect of natural climate fluctuations, the choice of wind  
946 dataset, the time period considered, and the methodologies and significance tests applied. The  
California Current Upwelling System (CCUS) is already heavily impacted by major emerging  
948 climate trends such as hypoxia and acidification, and strong remote forcing by natural climate  
fluctuations dominates near-decadal-scale wind trends and the associated ecosystem response.  
950 Therefore, the predicted human-induced long-term trend in upwelling winds, regardless of when  
it may occur, is and will be difficult to assess if these issues listed are not properly addressed.

952 We thus conducted a sensitivity study on the use of surface winds from recent model re-analyses  
and satellite analyses, using a choice of the period 1996-2018 for which satellite winds provide a  
954 reliable spatially-resolved wind dataset (both in speed and direction) and corresponding to a  
relatively neutral phase of the most important climate signals in the Pacific Ocean. In particular,  
956 we intend to highlight the essential role that satellite measurements can play as a reliable source  
of baseline data for the ongoing monitoring of the CCUS.

958 Over the period 1996-2018, which shows start end years not associated with particular phases of  
PDO, NPGO or ENSO, there is a trend of increasing upwelling-favorable winds in the core of the  
960 CCUS (approximately between Point Conception and Cape Blanco), obtained with the different  
datasets and methodologies used, and conflicting results are found in the southern CCUS between  
962 the satellite and model products. In the core of the CCUS, there is also good agreement on  
stronger equatorward winds for the winter and spring seasons between the different datasets.  
964 Increase in upwelling favorable winds in the CCUS core is associated with a local increase of  
more than 25% in the seasonal upwelling transport index, as found with satellite products. The  
966 observed spatial structuring of the estimated wind trends is consistent with the trend analysis of  
water chlorophyll-a, partial pressure of CO<sub>2</sub>, and basity (pH) analysis products.

968 However, systematic and time-dependent differences are found between the wind products,  
highlighting the need to further investigate the poorly documented temporal stability of these  
970 widely used wind climatology products. More sustained efforts are therefore needed to fully  
understand the differences between the analyzed datasets, some of which are likely due to  
972 artificial (non-physical) non-stationarity behavior or to systematic regional differences.

974

976 **Acknowledgments**

This study was conducted as part of the OceanSODA project, funded by the European Space  
978 Agency under the contract 4000112091/14/I-LG. The authors thank Antoine Grouazel for the  
production of the upwelling indices products, and the reviewers who helped to improve the  
980 manuscript.

982

**References**

984 Atlas, R., Hoffman, R.N., Ardizzone, J., Leidner, S.M., Jusem, J.C., Smith, D.K., Gombos, D.,  
2011. A cross-calibrated, multiplatform ocean surface wind velocity product for meteorological  
986 and oceanographic applications, *B. Amer. Meteorol. Soc.*, **92**, 157–174.

988 Bakun, A., 1973. Coastal upwelling indices, West Coast of North America, 1946–71. US  
Department of Commerce, National Oceanic and Atmospheric Administration, National Marine  
990 Fisheries Service.

992 Bakun, A., 1990. Global climate change and intensification of coastal ocean upwelling, *Science*,  
**247**, 198–201.

994

Bakun, A., Black, B.A., Bograd, S.J., et al., 2015. Anticipated Effects of Climate Change on  
996 Coastal Upwelling Ecosystems. *Curr. Clim. Change Rep.*, **1**, 85–93.  
<https://doi.org/10.1007/s40641-015-0008-4>.

998

Belmonte Rivas, M., Stoffelen, A., 2019. Characterizing ERA-interim and ERA5 surface wind  
1000 biases using ASCAT. *Ocean Sci.*, **15**. <https://doi.org/10.5194/os-15-831-2019>.

1002 Bentamy, A., Croize-Fillon, D., 2012. Gridded surface wind fields from Metop/ASCAT  
measurements. *Int. J. Remote Sens.*, **33**, 1729-1754. DOI 10.1080/01431161.2011.600348.

1004

Bograd, S. J. et al., 2009. Phenology of coastal upwelling in the California Current. *Geophys.*  
1006 *Res. Lett.*, **36**, L01602.

1008 Bonino, G., Di Lorenzo, E., Masina, S., et al., 2019. Interannual to decadal variability within and  
across the major Eastern Boundary Upwelling Systems. *Sci. Rep.*, **9**, 19949.  
1010 <https://doi.org/10.1038/s41598-019-56514-8>.

1012 Bourassa, M., Meissner, T., Cerovecki, I., Chang, P., Dong, X., De Chiara, G., et al., 2019.  
Remotely sensed winds and wind stresses for marine forecasting and ocean modeling. *Front.*  
1014 *Mar. Sci.*, **9**. <https://doi:10.3389/fmars.2019.00443>.

1016 Brady, R. X., Alexander, M. A., Lovenduski, N. S., & Rykaczewski, R. R., 2017. Emergent  
anthropogenic trends in California Current upwelling. *Geophys. Res. Lett.*, **44**, 5044-5052.

1018

Capet, X.J., Marchesiello, P., McWilliams, J.C., 2004. Upwelling response to coastal wind  
1020 profiles. *Geophys. Res. Lett.*, **31**, L13311. <https://doi:10.1029/2004GL020123>.

- 1022 Carvalho, D., Rocha, A., Gómez-Gesteira, M., Silva Santos, C., 2014. Comparison of reanalyzed,  
analyzed, satellite-retrieved and NWP modelled winds with buoy data along the Iberian Peninsula  
1024 coast. *Remote Sens. Environ.*, **152**, 480–492.
- 1026 Chan, F., Barth, J.A., Blanchette, C.A., et al., 2017. Persistent spatial structuring of coastal ocean  
acidification in the California Current System. *Sci. Rep.*, **7**, 2526. <https://doi.org/10.1038/s41598->  
1028 [017-02777-y](https://doi.org/10.1038/s41598-017-02777-y).
- 1030 Chau, T.T.T., Gehlen, M., Chevallier, F., 2020. Quality Information Document for Global Ocean  
Surface Carbon Product MULTIOBS\_GLO\_BIO\_CARBON\_SURFACE\_REP\_015\_008. CMEMS-  
1032 MOB-QUID-015-008, [https://resources.marine.copernicus.eu/documents/QUID/CMEMS-MOB-](https://resources.marine.copernicus.eu/documents/QUID/CMEMS-MOB-QUID-015-008.pdf)  
[QUID-015-008.pdf](https://resources.marine.copernicus.eu/documents/QUID/CMEMS-MOB-QUID-015-008.pdf)/ (accessed 19 April 2021).
- 1034
- Chavez, F.P., Pennington, J.T., Michisaki, R.P., Blum, M., Chavez, G.M., Friederich, J.,  
1036 Jones, B., Herlien, R., Kieft, B., Hobson, B., Ren, A.S., Ryan, J., Sevadjian, J.C., Wahl, C.,  
Walz, K.R., Yamahara, K., Friederich, G.E., Messié, M., 2017. Climate variability and  
1038 change: Response of a coastal ocean ecosystem. *Oceanography*, **30(4)**, 128–145.  
<https://doi.org/10.5670/oceanog.2017.429>.
- 1040
- Chelton, D., Xie, S.P., 2010. Coupled ocean-atmosphere interactions at oceanic mesoscales,  
1042 *Oceanography*, **23**, 52–69.

- 1044 Chenillat, F., Rivière, P., Capet, X., Di Lorenzo, E., Blanke, B., 2012. North Pacific Gyre  
Oscillation modulates seasonal timing and ecosystem functioning in the California Current  
1046 upwelling system. *Geophys. Res. Lett.*, **39**, L01606.
- 1048 Dee, D., and Coauthors, 2011. The ERA-Interim reanalysis: Configuration and performance of  
the data assimilation system. *Quart. J. Roy. Meteor. Soc.*, **137**, 553–597.
- 1050  
Denvil-Sommer A., Gehlen, M., Vrac, M., Mejia, C., 2019. LSCE-FFNN-v1: the reconstruction  
1052 of surface ocean pCO<sub>2</sub>. *Geosc. Model Dev.*, **12**, pp.2091-2105.
- 1054 Desbiolles, F. et al., 2017. Two decades [1992–2012] of surface wind analyses based on satellite  
scatterometer observations. *J. of Mar. Sys.*, **168**. <https://doi.org/10.1016/j.jmarsys.2017.01.003>.
- 1056  
Deutsch, C., Frenzel, H., McWilliams, J.C., Renault, L., Kessouri, F., Howard, Liang, J.H.,  
1058 Bianchi, D., 2020. Biogeochemical variability in the California Current System., *Progr.  
Oceanogr.* <https://doi.org/10.1101/2020.02.10.942565> , in press.
- 1060  
Di Lorenzo, E. and Coauthors, 2008. North Pacific Gyre Oscillation links ocean climate and  
1062 ecosystem change. *Geophys. Res. Lett.*, **35**, L08607. <https://doi.org/10.1029/2007GL032838>.
- 1064 Di Lorenzo, E., 2015. The future of coastal ocean upwelling. *Nature*, **518**, 310–311.  
<https://doi.org/10.1038/518310a>.
- 1066

Ding, H., Alexander, M. A., Jacox, M. G., 2021. Role of geostrophic currents in future changes  
1068 of coastal upwelling in the California Current System. *Geophys. Res. Lett.*, **48**, e2020GL090768.  
<https://doi.org/10.1029/2020GL090768>.

1070

Ekman, V.W., 1905. On the influence of the earth's rotation on ocean-currents. *Arkiv for*  
1072 *Matematik, Astronomy och Fysik* **2(11)**.  
<https://scholarship.library.jhu.edu/bitstream/handle/1774.2/33989/31151027498728.pdf?sequence=80&isAllowed=y> (accessed 19 April 2021)

1076 Estrade, P., Marchesiello, P., De Verdière, A.C., Roy, C., 2008. Cross-shelf structure of coastal  
upwelling : a two – dimensional extension of Ekman's theory and a mechanism for inner shelf  
1078 upwelling shut down. *J. Mar. Res.*, **66**, <http://dx.doi.org/10.1357/002224008787536790>.

1080 Feely, R.A., Sabine, C.L., Hernandez-Ayon, J.M., Ianson, D., Hales, B., 2008. Evidence for  
upwelling of corrosive “acidified” water onto the continental shelf. *Science*, **320**, 1490–1492.  
1082 <https://doi:10.1126/science.1155676>.

1084 García-Reyes, M., Largier, J., 2010. Observations of increased wind-driven coastal upwelling off  
central California, *J. Geophys. Res.*, **115**. <https://doi:10.1029/2009JC005576>.

1086

García-Reyes, M., Largier, J., 2012. Seasonality of coastal upwelling off central and northern  
1088 California: New insights, including temporal and spatial variability, *J. Geophys. Res.*, **117**.  
<https://doi:10.1029/2011JC007629>.

- 1090 García-Reyes, M., Sydeman, W. J., Schoeman, D. S., Rykaczewski, R. R., Black, B. A., Smit, A.  
1092 J., Bograd, S. J., 2015. Under pressure: Climate change, upwelling and eastern boundary  
upwelling ecosystems. *Front. Mar. Sci.*, **2**. <https://doi.org/10.3389/fmars.2015.00109>.
- 1094 Gruber, N., Hauri, C., Lachkar, Z., Loher, D., Frölicher, T. L., Plattner, G.-K., 2012. Rapid  
progression of ocean acidification in the California Current System. *Science*, **337**, 220–223.
- 1096 Halpern, D., 2002. Offshore Ekman transport and Ekman pumping off Peru during the 1997–  
1098 1998 El Niño. *Geophys. Res. Lett.*, **29**. <https://doi:10.1029/2001GL014097>.
- 1100 Hauri, C., Gruber, N., Vogt, M., Doney, S.C., Feely, R.A., Lachkar, Z., Leinweber, A.,  
McDonnell, A.M.P., Munnich, M., Plattner, G.K., 2013. Spatiotemporal variability and long-term  
1102 trends of ocean acidification in the California Current System. *Biogeosci.*, **10**, 193–216.  
<https://doi:10.5194/bg-10-193-2013>.
- 1104 Hersbach, H. , 2011. Sea-surface roughness and drag coefficient as function of neutral wind  
1106 speed. *J. Phys. Oceanogr.*, **41**, 247–251.
- 1108 Hersbach, H., and Coauthors, 2018. Operational global reanalysis: progress, future directions and  
synergies with NWP. *ECMWF Report Series*, **27**, ECMWF, Reading, UK.
- 1110 Hersbach, H., and Coauthors, 2020. The ERA5 global reanalysis. *Quarterly Journal of the Royal*  
1112 *Meteorological Society*, **146**, 1– 51. <https://doi.org/10.1002/qj.3803>.

1114 Hirsch, R. M., Slack, J. R., and Smith, R. A., 1982. Techniques of trend analysis for monthly  
water quality data, *Water Resour. Res.*, **18**,107–121. <https://doi.org/10.1029/WR018i001p00107>.

1116

Hirsch, R.M., Slack, J.R., 1984. A non-parametric trend test for seasonal data with serial  
1118 dependence, *Water Resour. Res.*, **20**, 727–732. <https://doi.org/10.1029/WR020i006p00727>.

1120 Iles, A. C. et al., 2012. Climate-driven trends and ecological implications of event-scale  
upwelling in the California Current System. *Glob. Change Biol.*, **18**, 783–796.

1122

Jacox, M. G., Moore, A. M., Edwards, C. A., Fiechter, J., 2014. Spatially resolved upwelling in  
1124 the California Current System and its connections to climate variability. *Geophys. Res. Lett.*, **41**,  
3189–3196.

1126

Jacox, M. G., Bograd, S. J., Hazen, E. L., & Fiechter, J., 2015. Sensitivity of the California  
1128 Current nutrient supply to wind, heat, and remote ocean forcing. *Geophys. Res. Lett.*, **42**, 5950-  
5957.

1130

Jacox, M. G., Hazen, E. L., & Bograd, S. J., 2016. Optimal environmental conditions and  
1132 anomalous ecosystem responses: Constraining bottom-up controls of phytoplankton biomass in  
the California Current System. *Scientific reports*, **6**, 27612.

1134

- Jacox, M. G., Edwards, C.A., Hazen, E.L., Bograd, S.J., 2018. Coastal upwelling revisited,  
1136 Ekman, Bakun, and improved upwelling indices for the U.S. West Coast. *J. Geophys. Res.*, **123**.  
<https://doi.org/10.1029/2018JC014187>.
- 1138
- Jackson, T., and co-authors, 2019. Ocean Colour Climate Change Initiative. *Product user guide*  
1140 *D3.4PUG*. <https://climate.esa.int/en/projects/ocean-colour/key-documents/> (accessed 19 April  
2021).
- 1142
- Kahru, M., Jacox, M. G., & Ohman, M. D., 2018. CCE1: decrease in the frequency of oceanic  
1144 fronts and surface chlorophyll concentration in the California Current System during the 2014-  
2016 northeast Pacific warm anomalies. *Deep Sea Research Part I: Oceanographic Research*  
1146 *Papers*, **140**, 4-13.
- 1148 Kent, E. C., Fangohr, S., and Berry, D. I., 2013. A comparative assessment of monthly mean  
wind speed products over the global ocean. *Inter. J. Climatol.* **33**, 2520–2541. [https://doi:](https://doi:10.1002/joc.3606)  
1150 [10.1002/joc.3606](https://doi:10.1002/joc.3606).
- 1152 Lachkar, Z., 2014. Effects of upwelling increase on ocean acidification in the California and  
Canary Current Systems. *Geophys. Res. Lett.*, **41**. <https://doi:10.1002/2013GL058726>.
- 1154
- Land, P.E., Shutler, J.D., Findlay, H.S., Girard-Ardhuin, F., Sabia, R., Reul, N., Piolle, J.-F.,  
1156 Chapron, B., Quilfen, Y., et al., 2015. Salinity from space unlocks satellite-based assessment of  
ocean acidification. *Environ. Sci. Tech.* **49**, 987–1,994, <http://dx.doi.org/10.1021/es504849s>.

1158

Land, P.E., Findlay, H.S., Shutler, J.D., Ashton, I., Holding, T., Grouazel, A., Arduin, F., Reul,  
1160 N., Piolle, J.-F., Chapron, B., Quilfen, Y., et al., 2019. Optimum satellite remote sensing of the  
marine carbonate system using empirical algorithms in the global ocean, the Greater Caribbean,  
1162 the Amazon Plume and the Bay of Bengal. *Remote Sens. Environ.*, **235**.  
[https://doi :10.1016/j.rse.2019.111469](https://doi.org/10.1016/j.rse.2019.111469).

1164

Marchesiello, P., Estrade, P., 2010. Upwelling limitation by onshore geostrophic flow. *J. Mar.*  
1166 *Res.*, **68**, p. 37-62. ISSN 0022-2402.

1168 Mears, C. A., Scott, J., Wentz, F. J., Ricciardulli, L., Leidner, S. M., Hoffman, R., Atlas, R.,  
2019. A Near-Real-Time Version of the Cross-Calibrated Multiplatform (CCMP) Ocean Surface  
1170 Wind Velocity Dataset. *J. Geophys. Res.*, **124**. <https://doi.org/10.1029/2019JC015367>.

1172 Meinvielle, M., Johnson, G.C., 2013. Decadal water-property trends in the California  
Undercurrent, with implications for ocean acidification. *J. Geophys. Res. Oceans*, **118**, 6687–703.

1174

Narayan, N., Paul, A., Mulitza, S., Schulz, M., 2010. Trends in coastal upwelling intensity during  
1176 the late 20th century. *Ocean Sci.* **6**, 815–823.

1178 Pickett, M. H., Paduan, J.D., 2003. Ekman transport and pumping in the California Current based  
on the U.S. Navy's high-resolution atmospheric model (COAMPS). *J. Geophys. Res.*, **108**.  
1180 <https://doi:10.1029/2003JC001902>.

Quilfen, Y., Chapron, B., Vandemark, D., 2001. The ERS scatterometer wind measurement  
1182 accuracy: Evidence of seasonal and regional biases. *J. Atmos. Ocean. Tech.*, **18**, 1684-1697.  
[https://doi.org/10.1175/1520-0426\(2001\)018<1684:TESWMA>2.0.CO;2](https://doi.org/10.1175/1520-0426(2001)018<1684:TESWMA>2.0.CO;2).

1184

Quilfen, Y., Chapron, B., Collard, F., Vandemark, D., 2004. Relationship between ERS  
1186 scatterometer measurement and integrated wind and wave parameters. *J. Atmos. Ocean. Tech.*, **21**,  
368-373. [https://doi.org/10.1175/1520-0426\(2004\)021<0368:RBESMA>2.0.CO;2](https://doi.org/10.1175/1520-0426(2004)021<0368:RBESMA>2.0.CO;2).

1188

Renault, L., Hall, A., McWilliams, J.C., 2015. Orographic shaping of U.S. West Coast wind  
1190 profiles during the upwelling season. *Climate Dyn.*, **46**, 273–289. <https://doi.org/10.1007/s00382-015-2583-4>.

1192

Renault, L., Deutsch, C., McWilliams, J.C., 2016. Partial decoupling of primary productivity  
1194 from upwelling in the California Current system. *Nature Geosc.*, **9**, 505–508.  
<https://doi.org/10.1038/ngeo2722>.

1196

Rykaczewski, R.R., Checkley, D.M., 2008. Influence of ocean winds on the pelagic ecosystem in  
1198 upwelling regions. *Proc. Natl. Acad. Sci.*, **105**, 1965–70.

1200 Rykaczewski, R.R., Dunne, J.P., Sydeman, W.J., García-Reyes, M., Black, B.A., Bograd, S.J.,  
2015. Poleward displacement of coastal upwelling-favorable winds in the ocean's eastern  
1202 boundary currents through the 21st century, *Geophys. Res. Lett.*, **42**, 6424–6431.  
<https://doi:10.1002/2015GL064694>.

1204

Sen, P. K., 1968. Estimates of the regression coefficient based on Kendal's Tau. *J. Am. Stat.*

1206 *Assoc.*, **63**, 1379–1389. <https://doi:10.1080/01621459.1968.10480934>.

1208 Serinaldi, F., Kilsby, C.G., Lombardo, F., 2018. Untenable non-stationarity: An assessment of the fitness for purpose of trend tests in hydrology. *Adv. Water Resour.*, **111**, 132-155.

1210 <https://doi.org/10.1016/j.advwatres.2017.10.015>.

1212 Shutler, J.D., Wanninkhof, R., Nightingale, P.D., Woolf, D.K., Bakker, D.C.E., Watson, A., Ashton, I., Holding, T., Chapron, B., Quilfen, Y., et al., 2019. Satellites will address critical

1214 science priorities for quantifying ocean carbon. *Front. Ecol. Environ.*, **18**, 27-35.

1216 Sydemann, W. J. et al., 2014. Climate change and wind intensification in coastal upwelling ecosystems. *Science*, **345**, 77–80.

1218

Taboada, F. G., Stock, C. A., Griffies, S. M., Dunne, J., John, J. G., Small, R. J., & Tsujino, H.,

1220 2019. Surface winds from atmospheric reanalysis lead to contrasting oceanic forcing and coastal upwelling patterns. *Ocean Modelling*, **133**, 79-111.

1222

Turi, G., Lachkar, Z., Gruber, N., Münnich, M., 2016. Climatic modulation of recent trends in

1224 ocean acidification in the California Current System. *Envir. Res. Lett.*, **11**, 014007.

1226 Young, I. R., Ribal, A., 2019. Multiplatform evaluation of global trends in wind speed and wave  
height. *Science*, **364**, 548–552.

1228

Wang, D., Gouhier, T., Menge, B. *et al.*, 2015. Intensification and spatial homogenization of  
1230 coastal upwelling under climate change. *Nature*, **518**, 390–394.  
<https://doi.org/10.1038/nature14235>

1232

Wang, Y.H., Walter, R.K., White, C., Farr, H.K., Ruttenberg, B.I., 2019. Assessment of surface  
1234 wind datasets for estimating offshore wind energy along the Central California Coast. *Renew.*  
*Energy*, **133**, 343-353. <https://doi.org/10.1016/j.renene.2018.10.008>

1236

1238

1240

1242

1244

1246

1248

## Appendix A

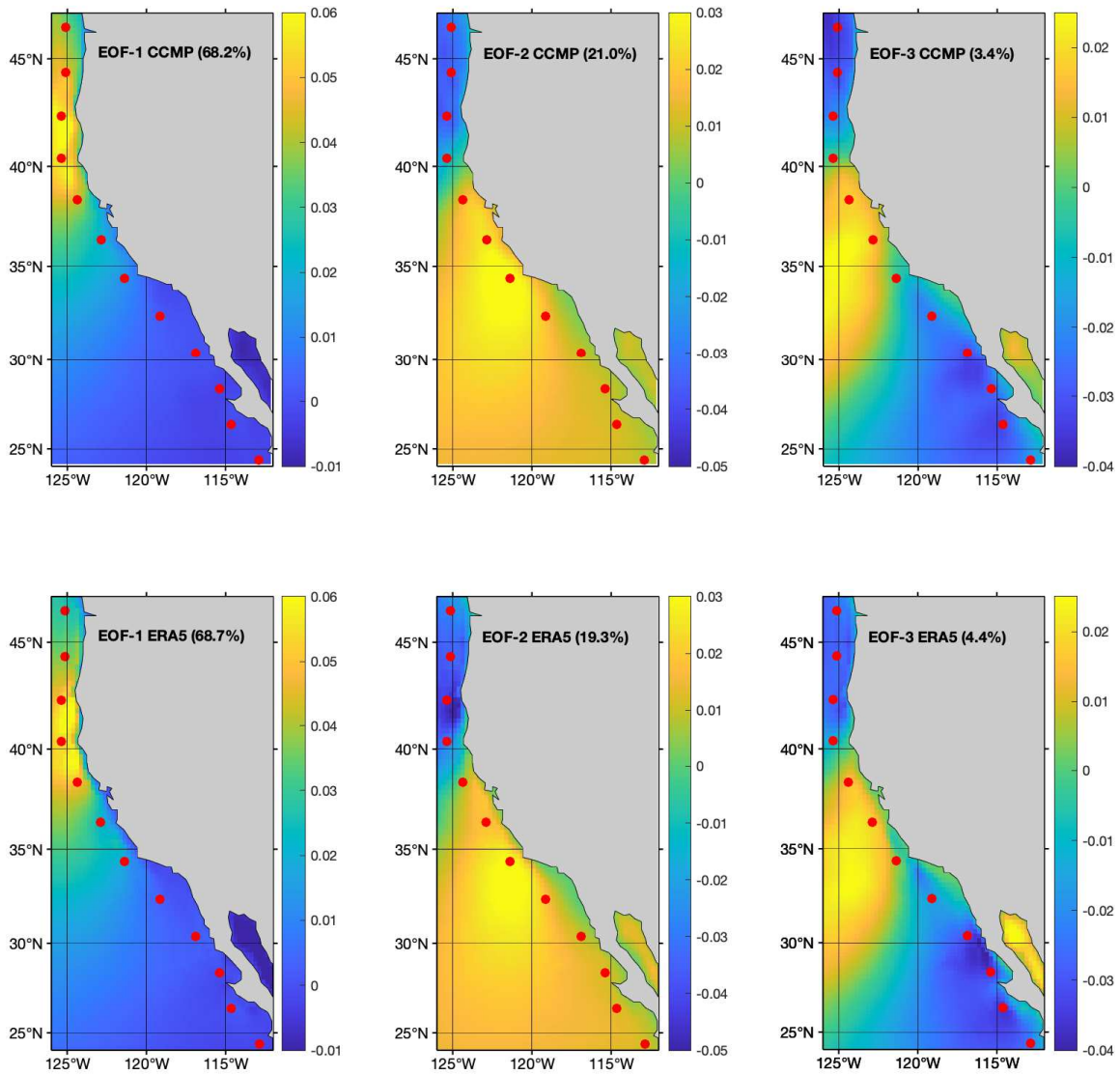
1250

**Table 1** : For the twelve stations, one by row, shown in Figure 2, from left to right column:

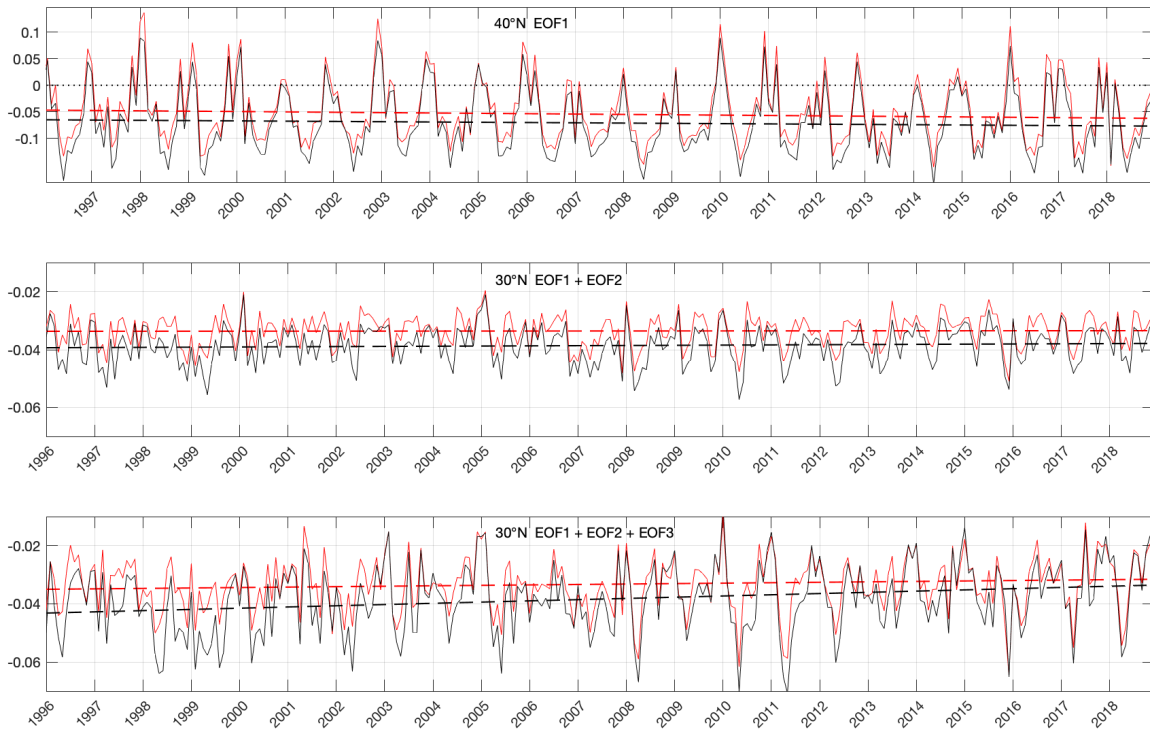
1252 station number, longitude (degree), latitude (degree), distance to coast (D2coast, km), seafloor depth (m), coast angle (degree, anticlockwise from the eastward axis).

Station number	Longitude (degrees)	Latitude (degrees)	D2coast (km)	Depth (m)	Coast angle (degrees)
1	-112.875	24.375	101	2827	122
2	-114.625	26.375	93	3476	138
3	-115.375	28.375	103	342	138
4	-116.875	30.375	81	2364	114
5	-119.125	32.375	178	343	142
6	-121.375	34.375	97	2454	125
7	-122.875	36.375	95	3140	104
8	-124.375	38.375	93	3730	124
9	-125.375	40.375	98	1807	92
10	-125.375	42.375	83	3078	93
11	-125.125	44.375	88	1099	82
12	-125.125	46.375	92	1592	109

1254



1258 Figure A1: First three EOFs of the meridional wind stress component for CCMP (top) and ERA5  
 (bottom). Red dots give the location of the 12 stations. The percentage of variance accounted for  
 1260 by the first three EOFs is 68.7, 19.3, 4.4 for ERA5; 68.2, 21.0, 3.4 for CCMP.



1262

Figure A2: Time series at station 9 (40°N, top panel) and station 4 (30°N, center and bottom panels) of the meridional wind stress EOF components ( $\text{N}\cdot\text{m}^{-2}$ , solid lines) and associated estimated trend lines (dashed lines) for CCMP (red) and ERA5 (black).

1264

1266 At 40°N, station 9, the percentage of variance accounted for by EOF1 is 91.5% and 95.4% for ERA5 and CCMP, respectively.

1268

At 30°N, station 4, the percentage of variance accounted for by the first three EOFs is 5.2, 21.0, 56.0 for ERA5 and 0.2, 27.6, 49.5 for CCMP. The meridional wind stress component is reconstructed with the two first EOFs (center panel), and with the three first EOFs (bottom panel). See section 2.2 for discussion.

1272

1274

## List of Figures Captions

1276

**Figure 1.** Taylor diagrams for comparison of CMEMS (left panels), ERAInterim (center panels),  
1278 ERA5 (right panels)  $\tau_{upw}$  with the CCMP data. The radial axis represents the normalized  
standard deviation (STD), with the unit value referenced as the CCMP STD; the root mean  
1280 square differences (RMSD) with respect to the CCMP data are represented by green dashed arcs  
and numbers ( $Nm^{-2}$ ); the correlation coefficients vary in the azimuthal direction as blue dashed-  
1282 dotted lines and numbers; and the diamonds are color-coded according to the mean bias with  
respect to the CCMP ( $Nm^{-2}$ ). Top: 1996-2006; Bottom 2007-2018.

1284

**Figure 2.** Location of the twelve stations (dots) and seafloor elevation (left, m), mean Ekman  
1286 vertical velocity (center,  $ms^{-1}$ , zero-contour as a magenta solid line), and mean Ekman transport  
(right,  $m^2s^{-1}$ , black arrows indicate the orientation of the coastline used to derive  $\tau_{upw}$ )

1288

**Figure 3.** Monthly values of climate indices: top, North Pacific Gyre Oscillation (NPGO) index,  
1290 center, Pacific Decadal Oscillation (PDO) index, bottom, multivariate El Niño Southern  
Oscillation (ENSO) index.

1292

**Figure 4.** top panel: trends in Chl-a ( $mg\ m^{-3}\ yr^{-1}$ ) nearshore (distance to coast  $< 50$  km, red solid  
1294 line) and offshore ( $75\ km < distance\ to\ coast < 150$  km, blue solid line) for the period 1998-2018.  
Central and bottom panels: trends in  $pCO_2$  (central panel,  $0.1Pa\ yr^{-1}$ ) and pH (bottom panel) for  
1296 the periods 1998-2018 (red solid line) and 1985-2018 (blue solid line). The colored areas  
correspond to a p-value  $< 0.1$ .

1298 **Figure 5.** Monthly values of coastal Chl-a ( $\text{mg m}^{-3}$ , averaged over a distance to coast  $< 50$  km)  
for the periods 1998-2018, and seasonal values such as: December/January/February (DJF, blue  
1300 line), April/May/June (AMJ, green line), July/August/September (JAS, red line).  
March/October/November (MON, black line). The dashed black lines show the trend as  
1302 estimated in Figure 4. The latitude shown in the upper left corner of each plot is the latitude of  
the coastal point located on the perpendicular to stations 1, 3, 5, 7, 9, 11 from bottom-right to top-  
1304 left (see Table A1 for details).

1306

**Figure 6.** Top panels: Annual  $\tau_{\text{upw}}$  trends ( $\text{N.m}^{-2}$  per year, negative for increasing equatorward  
1308 winds) as a function of latitude, for the twelve stations, over the period 1996-2018, for model  
winds (left panel) and satellite winds (right panel). The color-shaded areas correspond to p-value  
1310  $< 0.1$ . Bottom panels: Seasonal  $\tau_{\text{upw}}$  trends ( $\text{N.m}^{-2}$  per year) over the same period and on the  
same x-axis for model winds (left panel) and satellite winds (right panel), for the winter season  
1312 (solid lines), the upwelling season (dashed lines), and the transition season (dashed-dotted lines).  
Filled squares indicate  $p < 0.1$ . The color code follows ERA5 in black, ERAI in blue, CMEMS in  
1314 red, CCMP in green.

1316 **Figure 7.** Top panel: average integrated Ekman pumping transport ( $\text{m}^3\text{s}^{-1}$  per 100m of coast) as a  
function of latitude, for the twelve stations, averaged over the 1996-2018 period. Lower panel:  
1318 associated trends ( $\text{m}^3\text{s}^{-1}$  per year) over the same period and same x-axis for ERA5 in black,  
CMEMS in red, CCMP in green.

1320

**Figure 8.** Mean alongshore upwelling winds ( $\tau_{upw}$ ,  $N.m^{-2}$ , negative when equatorward) and associated CUI ( $m^{-3}.s^{-1} / 100m$ ) as a function of time, at  $116^{\circ}875W - 30^{\circ}375N$  (top panels) and  $125^{\circ}375W - 40^{\circ}375N$  (bottom panels). The color code follows ERA5 in black, CMEMS in red, CCMP in green, ERAInterim in blue.

1326

**Figure 9.** Total Upwelling Magnitude Index (TUMI,  $m^{-3}.s^{-1}$  per 100m) as a function of time at  $116^{\circ}875W - 30^{\circ}375N$ , first top panel, and  $125^{\circ}375W - 40^{\circ}375N$ , second top panel. For  $125^{\circ}375W - 40.375^{\circ}N$  the associated upwelling season length (number of days, first lower panel), and day of upwelling season start in each year (second lower panel). Dashed lines in top panels show the trends obtained with the SKTT method. The color code follows ERA5 in black, ERAI in blue, CMEMS in red, CCMP in green.

1334

**Figure A1.** First three EOFs of the meridional wind stress component for CCMP (top) and ERA5 (bottom). Red dots give the location of the 12 stations. The percentage of variance accounted for by the first three EOFs is 68.7, 19.3, 4.4 for ERA5; 68.2, 21.0, 3.4 for CCMP.

1338

**Figure A2.** Time series at station 9 ( $40^{\circ}N$ , top panel) and station 4 ( $30^{\circ}N$ , center and bottom panels) of the meridional wind stress EOF components ( $N.m^{-2}$ , solid lines) and associated estimated trend lines (dashed lines) for CCMP (red) and ERA5 (black).

1342

At 40°N, station 9 , the percentage of variance accounted for by EOF1 is 91.5% and 95.4% for  
1344 ERA5 and CCMP, respectively.

At 30°N, station 4, the percentage of variance accounted for by the first three EOFs is 5.2, 21.0,  
1346 56.0 for ERA5 and 0.2, 27.6, 49.5 for CCMP. The meridional wind stress component is  
reconstructed with the two first EOFs (center panel), and with the three first EOFs (bottom  
1348 panel). See section 2.2 for discussion.

1350

1352